

FASHI: A search for extragalactic OH megamasers with FASTCHUAN-PENG ZHANG,^{1,2} CHENG CHENG,³ MING ZHU,^{1,2} AND PENG JIANG^{1,2}¹*National Astronomical Observatories, Chinese Academy of Sciences, Beijing 100101, China*²*Guizhou Radio Astronomical Observatory, Guizhou University, Guiyang 550000, China*³*Chinese Academy of Sciences South America Center for Astronomy, National Astronomical Observatories, CAS, Beijing 100101, China*

ABSTRACT

The **F**AST **A**ll **S**ky **H**I survey (FASHI) is broader in frequency band and deeper in detection sensitivity than the Arecibo Legacy Fast ALFA survey (ALFALFA). FASHI is designed to cover the entire sky observable by the Five-hundred-meter Aperture Spherical radio Telescope (FAST). To efficiently expand the OH megamaser (OHM) sample at the rest frequency of 1667.35903 MHz, we directly matched the IRAS Point Source Catalog Redshift (PSCz) catalog with the corresponding FASHI data cube. We then obtained 27 OHMs, including 9 previously known and 18 new ones, within a redshift range of $0.14314 \lesssim z_{\text{OH}} \lesssim 0.27656$. We also measured the hyperfine ratio of nine OHMs between the 1667 and 1665 MHz lines. The ratio ranges from 1.32 to 15.22, with an average of $R_{1667:1665} = 4.74$. To fit the L_{OH} and L_{FIR} relationship, we have $\log L_{\text{OH}} = (1.58 \pm 0.10) \log L_{\text{FIR}} - (15.93 \pm 1.20)$, which is almost the same as the previous observations. All 27 OHMs have relatively high FIR luminosities, suggesting that the host system has undergone a very recent and violent starburst. The multi-wavelength SED fitting results also show that the OH host galaxies are massive ($M_* \simeq 10^{11} M_{\odot}$) galaxies with the SFR above the star-forming main sequence. The high A_V value of the OH galaxies from the SED fit is consistent with the high IR luminosities. On the other hand, not all ULIRGs have detectable OH emission, suggesting that the OH emission may be triggered within a specific stage of the merger. In general, FAST, with its 19-beam array and UWB receiver, will be a powerful tool for observing more OHMs and unraveling their mystery in the future.

Keywords: Radio telescopes (1360), Megamasers (1023), Hydroxyl masers (771), Redshift surveys (1378), Radio sources (1358)

1. INTRODUCTION

OH megamasers (OHMs) at rest frequencies of 1667 and 1665 MHz in extragalactic systems are valuable indicators of galaxy interactions. These megamasers are thought to originate from the starburst nuclei of merging gas-rich galaxy systems, based on both high-resolution interferometer observations (Lo 2005) and statistical analysis of luminosity functions (Darling & Giovanelli 2002, 2006; Giovanelli & Haynes 2015). OHMs thus offer a distinctive approach to measuring the occurrence of galaxy mergers at specific evolutionary stages. (Lo 2005). The masing emission or absorption lines are usually broad, with a line width ranging from 10 to 10^3 km s^{-1} , and exhibit an isotropic luminosity in the range of $10 - 10^4 L_{\odot}$ (Darling & Giovanelli 2002).

OHMs are connected to high-density molecular gas ($n(\text{H}_2) \sim 10^4 \text{ cm}^{-3}$) and strong far-infrared radiation. They would offer potential insights into extreme star formation and galactic evolution, particularly high-redshift OHMs (Darling 2007; Lockett & Elitzur 2008; Roberts et al. 2021; Glowacki et al. 2022; Jarvis et al. 2023). Therefore, investigating OHMs is a meaningful pursuit.

As of now, approximately 135 OHMs have been discovered, for instance, in studies of Darling & Giovanelli (2002); Willett (2012); Haynes et al. (2018); Suess et al. (2016); Hess et al. (2021); Roberts et al. (2021); Glowacki et al. (2022); Jarvis et al. (2023). The Arecibo Sky Survey exhibits the most successful tracking or single-point observation to date, detecting approximately 17% of OHMs (Darling & Giovanelli 2000). All OHMs known to date are exclusively associated with (ultra)luminous infrared galaxies ([U]LIRGs), even those with $L_{\text{FIR}} \gtrsim 10^{12} L_{\odot}$ (Baan 1991). However, only about 20% of [U]LIRGs are detected with OHM emission, as shown by studies conducted by Baan (1991);

Baan et al. (1992); Darling & Giovanelli (2000, 2001, 2002). The production of OHMs may be a transient phenomenon in the evolution of a galaxy, from starburst nucleus to an AGN (Wiggins et al. 2016), or has beaming and orientation effects, as suggested in Darling (2007).

The Five-hundred-meter Aperture Spherical radio Telescope (FAST) All Sky HI survey (FASHI) aims to cover the entire sky visible to FAST, between declinations of -14° and $+66^\circ$, within a frequency range of $1.0 - 1.5$ GHz (Nan et al. 2011; Jiang et al. 2019, 2020). The survey currently has a typical map rms of ~ 0.76 mJy beam $^{-1}$ with a velocity resolution of 6.4 km s $^{-1}$ within a redshift range of $0.11 - 0.66$ for OHMs (Zhang et al. 2024), while the Arecibo Legacy Fast ALFA Survey (ALFALFA) has a lower detection sensitivity of ~ 1.86 mJy beam $^{-1}$ after smoothing to a velocity resolution of 10 km s $^{-1}$ (Haynes et al. 2018). This suggests that the FASHI could detect more OHMs than the ALFALFA. Furthermore, the Ultra-Wide Bandwidth (UWB) receiver on FAST can simultaneously cover a frequency range of 500 – 3300 MHz (or $z < 2.33$), making FAST a powerful instrument for observing the OHMs in extragalactic objects (Zhang et al. 2023).

In this paper, we mainly report 18 new and 9 old OHMs detected by FAST. Section 2 shows the FAST observations and source identification. Section 3 presents the characterization of the detected OHMs and lists four OHM-related catalogs. Section 4 discusses the hyperfine ratio, host galaxy properties, L_{OH} and L_{FIR} relationship, and FAST OHM detectability. Section 5 is a summary. Throughout this paper, we assume a Λ CDM cosmology with $H_0 = 75$ km s $^{-1}$ Mpc $^{-1}$, $\Omega_M = 0.3$, and $\Omega_\Lambda = 0.7$.

2. DATA AND IDENTIFICATION

2.1. Observational data

The observational spectral data are from the FASHI project by Zhang et al. (2024), using the FAST 19-beam receiver to efficiently cover the FAST sky. The aperture of FAST is 500 m and the effective aperture is about 300 m, resulting in a beam size of $\sim 2.9'$ at 1.4 GHz. The full broadband of 500 MHz in the spectral line backend has a frequency coverage of 1000 to 1500 MHz with a total of 64k channels. The corresponding frequency resolution is 7.63 kHz or 1.6 km s $^{-1}$ at 1.4 GHz. The FASHI data are reduced using the FAST spectral data reduction pipeline HiFAST¹. The HiFAST pipeline combines data reduction packages including antenna temperature

correction, baseline correction, RFI mitigation, standing wave correction, gridding, flux correction, and fit cube generation. The data has been smoothed to 6.4 km s $^{-1}$ spectral resolution per channel and the fit cubes are gridded to a pixel scale of $1'$. A heliocentric velocity correction was applied to the data due to the Doppler effect. A detailed observational setup and data reduction procedure is presented in the FASHI paper by Zhang et al. (2024).

2.2. Source identification

The extragalactic HI and OHM lines have a similar spectral profile at different redshifts. Spectroscopic redshift information is needed to distinguish them (Hess et al. 2021). The IRAS Point Source Catalog Redshift (PSCz) survey consists of spectroscopic redshifts, infrared and optical photometry, and miscellaneous information for 18351 IRAS sources, mostly selected from the Point Source Catalog (Saunders et al. 2000). The survey covers almost all galaxies with flux brighter than 0.595 Jy at 60 microns, over the 84% of the sky. It is well known that most previously known OHM have associated IRAS sources (e.g., Darling & Giovanelli 2000, 2001, 2002). To efficiently expand the OHM sample, we could directly cross-check the PSCz catalog (Saunders et al. 2000) with the corresponding FASHI data cube to see if there are any emission lines within a beam size of $2.9'$ and a velocity range of ~ 600 km s $^{-1}$. The FASHI data covers around 10000 deg 2 within $0^h \lesssim \text{RA} \lesssim 17^h$, $22^h \lesssim \text{RA} \lesssim 24^h$, $6^\circ \lesssim \text{DEC} \lesssim 0^\circ$, and $18^\circ \lesssim \text{DEC} \lesssim 64^\circ$ with a typical spectral detection sensitivity of ~ 1.50 mJy with a velocity resolution of ~ 6.4 km s $^{-1}$ at 1.4 GHz. Because the FASHI project can only operate in schedule-filler mode, parts of the above region are not fully covered. Within the region we found that there are a total of 145 PSCz sources covered by the current FASHI data with the spectroscopic redshifts in the frequency range from 1304 to 1461 MHz. Using the FAST spectral data and the moment 0 , 1 , 2 images, we check the 145 sources one by one, including the redshift, coordinate, flux density, and the g , r , and z bands of the SDSS data, and then discard the probable HI source. In the end, we discovered and conformed 27 OHMs, 18 of which were first found by FAST. Detailed information on these sources is presented in the following sections.

3. DETECTION RESULTS AND ANALYSIS

3.1. OHM locations

In Figure 1 we show all the OHM locations, including 18 new OHMs found by FAST and 135 known ones found by others. From the Figure 1 we can see

¹ <https://hifast.readthedocs.io/>

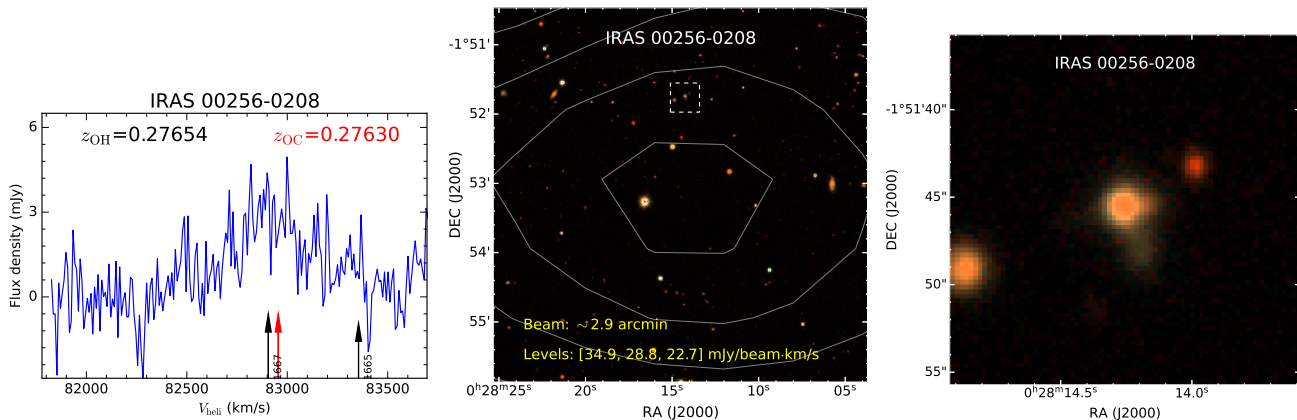


Figure 2. OHM IRAS 08201+2801. *Left:* FAST detected OH emission spectrum. The 1667 MHz OH redshift measured by FAST (in black) and a spectroscopic redshift (in red) are presented above and below the spectrum with text and corresponding colored arrows, respectively. The velocity position of the expected 1665 MHz OH line is indicated by a shorter arrow. *Middle:* Gray contours indicate the OH integrated intensity distribution by FAST with a beam size of $\sim 2.9'$. The first three contour levels from inner to outer are shown in the image. The background shows an RGB image of the g , r , and z bands of the SDSS data. The white square indicates the optical counterpart (OC) of the OHM. *Right:* The zoomed-in RGB image of the OC within the white square in the middle panel. The figures for the other 26 OHMs are shown in the Appendix.

This OHM was first found and reported by the Arecibo OHM Surveys (Darling & Giovanelli 2000). The 1667 MHz peak flux density observed by FAST is consistent with that of (Darling & Giovanelli 2000). The strong corresponding 1665 MHz line is also visible. The measured line ratio is $R_{1667:1665} = 3.27 \pm 0.63$ (see Tables 2). This source has been proposed as a composite of H II and LINER features based on the Osterbrock spectral line ratio classification method (Osterbrock 1989; Veilleux et al. 1995). The optical RGB image is unresolved, but there may be another nucleus or tidal tail to the north of the main nucleus.

3.2.6. IRAS 08201+2801

IRAS 08201+2801 has been confirmed as an OHM by the Arecibo OHM Surveys (Darling & Giovanelli 2001). This object was also detected by the FASHI survey. The coordinates and redshift are very close between the two observations, but the OH line profile observed by FAST is consistent with that of Darling & Giovanelli (2001). The measured OH and infrared parameters are listed in Tables 1 and 3. The FIR luminosity of this object is $10^{11.98 \pm 0.03} L_{\odot}$ and it belongs to a LIRG galaxy. Kim et al. (1998) classified the nucleus of this LIRG as a starburst. The OH spectrum of 08201+2801 shows multiple velocity components with $W_{50} = 242.3 \text{ km s}^{-1}$. In Figure 10, the optical RGB image shows an obvious morphology with two nuclei connected by arcs and a single kinked tidal tail, clearly indicating an advanced merger (see also Darling & Giovanelli 2001).

3.2.7. IRAS 08328+5148

The OHM IRAS 08328+5148 was first found and identified by the FASHI survey (see Figures 11). At the eastern position (named OC-1 with RA, DEC = 129.1717° , 51.6246°) of the currently identified OC, there is an optical spectroscopic object with a redshift of 0.237 from the SDSS catalog. However, the OC coordinates are $48''$ away from the OH emission center measured by FASHI. Fortunately, we find another optical object (named OC-2 with RA, DEC = 129.1505° , 51.6267°) at the center of the OH emission distribution. Although this object has no spectroscopic redshift, its SDSS photometric redshift is 0.234 ± 0.070 , which agrees well with the OH redshift of 0.23749. In addition, OC-1 and OC-2 have a similar optical color feature. Furthermore, the coordinates of IRAS 08328+5148 are in good agreement with the observed OH line coordinates. Therefore, it is likely that the OC-2 is the optical counterpart of this OHM, but its spectroscopic redshift is needed for further confirmation. The FIR luminosity is $L_{\text{FIR}} = 10^{12.05 \pm 0.05} L_{\odot}$, which belongs to a ULIRG. The OH and infrared parameters are listed in Tables 1 and 3. The optical RGB image shows a possible merging system with a visible tidal tail. The OH spectrum shows multiple velocity components, indicating an active merging process.

3.2.8. IRAS 08566-0252

The OHM IRAS 08566-0252 was first found and identified by the FASHI survey (see Figures 12). Its measured OH redshift is 0.20262, while the optically observed redshift is 0.20201 (Saunders et al. 2000) (see Tables 1 and 3). Their velocity difference is $\sim 400 \text{ km s}^{-1}$, but spatially the two are in good agreement. A careful search for other optical objects shows that there is no

possible match to the radio observation. There is a weak emission line ($< 3\sigma$) at the position of the corresponding 1665 MHz line. More integration time is needed to verify its authenticity. The optical RGB image shows a possible merging system with two close nuclei. The OH spectrum shows multiple velocity components, indicating an active merging process.

3.2.9. *IRAS 10106+4708*

The OHM IRAS 10106+4708 was first discovered by the FASHI survey (see Figures 13). The optical coordinates and the spectroscopic redshift ($z_{\odot} = 0.20481$; Saunders et al. 2000) are in good agreement with the observed OH line coordinates and redshift ($z_{\odot} = 0.20529$) for this object. The strong sharp peak of the OH line is 24.73 ± 1.32 mJy. The OH luminosity is $L_{\text{OH}} = 10^{3.67 \pm 0.01} L_{\odot}$ (see Table 1). IRAS 10106+4708 has a FIR luminosity of $L_{\text{FIR}} = 10^{12.04 \pm 0.05} L_{\odot}$ (see Table 3), which belongs to a ULIRG. In Figure 13, the optical RGB image shows a compact nucleus with extended tidal tails. The object is bright in all four WISE bands, and the optical data display an evident tidal tail. Despite that, the optical extinction is significant, leading to the absence of the H β and [OIII] lines. The WISE color at ([4.6]-[12], [3.4]-[4.6]) is approximately estimated to be (4.18, 0.86) based on the WISE flux. As a result, this object is speculated to be a dusty quasar (Nikutta et al. 2014). The measured OH and infrared parameters are listed in Tables 1 and 3.

3.2.10. *IRAS 10558+3845*

The OHM IRAS 10558+3845 was first found and identified by the FASHI survey (see Figures 14). Its measured OH redshift is 0.20788, while the optically observed redshift is 0.20660 (Saunders et al. 2000) (see Tables 1 and 3). The velocity difference is ~ 400 km s $^{-1}$, but spatially the two are in good agreement. A careful search for other optical objects shows that there is no possible match to the radio observation. The optical RGB image shows an apparent spiral tidal tails surrounding the nucleus. The OH spectrum shows multiple velocity components, indicating an active merging process. The velocity position of the 1665 MHz line shows a weak emission profile. The measured line ratio is $R_{1667:1665} = 1.62 \pm 0.52$.

3.2.11. *IRAS 10597+5926*

This OHM is first found and reported by (Willett 2012), where the detected peak flux density is 17.56 mJy, while it is 32.27 ± 2.23 mJy measured by FAST. The both flux densities have large difference. However, the line profiles are consistent between the two. We also

detected the 1665 MHz emission. The measured line ratio is $R_{1667:1665} = 15.22 \pm 1.46$ between the 1667 and 1665 MHz lines. The optical RGB image shows a possible merging system with interacting activity. The OH spectrum shows strong and multiple velocity components, indicating an active merging process.

3.2.12. *IRAS 11029+3130*

This OHM was first found and reported by the Arecibo OHM surveys (Darling & Giovanelli 2001). The line profile and flux density observed by FAST are in good agreement with that of (Darling & Giovanelli 2001). The only difference is that Darling & Giovanelli (2001) identified it as the name of IRAS 11028+3130, which is not listed in the PSCz catalog compiled by Saunders et al. (2000). The central core is a LINER-type active galaxy nucleus (Alatalo et al. 2016). The optical RGB image is unresolved (see Figure 16), but there is an extended structure to the west of the main nucleus. This may be probably indicative of an active merging system.

3.2.13. *IRAS 11087+5351*

The OHM IRAS 11087+5351 was first discovered by the FASHI survey (see Figures 17). The optical coordinates and the spectroscopic redshift ($z_{\odot} = 0.14270$; Saunders et al. 2000) are in good agreement with the observed OH line velocities ($z_{\odot} = 0.14314$) and spatial coordinates. The 1665 MHz emission line is clearly visible. The measured line ratio is $R_{1667:1665} = 1.32 \pm 0.21$, which is the measured lowest ratio among all sources in this work. In Figure 17, the optical RGB image shows an extended morphology with a bright nucleus in the center that may be indicative of interaction. The central nucleus is identified as a LINER-type active galaxy nucleus by (Toba et al. 2014). The OH and infrared parameters are listed in Tables 1 and 3.

3.2.14. *IRAS 11161+6020*

The OHM IRAS 11161+6020 was first discovered by the FASHI survey (see Figures 18). The optical coordinates and spectroscopic redshift ($z_{\odot} = 0.26428$; Abazajian et al. 2009) are in good agreement with the observed OH line coordinates and redshift ($z_{\odot} = 0.26434$). The OH luminosity is $L_{\text{OH}} = 10^{3.68 \pm 0.02} L_{\odot}$ (see Table 1). It has a FIR luminosity of $L_{\text{FIR}} = 10^{12.21 \pm 0.04} L_{\odot}$ (see Table 3), which belongs to a ULIRG. Toba et al. (2014) classified it spectroscopically as a Seyfert 2 galaxy. In Figure 18 the optical RGB image shows a compact nucleus with complex tidal tails. The OH spectrum has multiple velocity components, probably due to the interaction in the merger process.

3.2.15. *IRAS 11301-0523*

The OHM IRAS 11301-0523 was first discovered by the FASHI survey (see Figures 19). The optical spectroscopic redshift ($z_{\odot} = 0.23019$; Saunders et al. 2000) is in good agreement with the observed OH redshift ($z_{\odot} = 0.22984$). The spatial coordinate offset between them is $\sim 1'$. In Figure 18 the optical RGB image shows an arc-like structure with several close and connected nuclei, which may be an interacting merging system. The OH spectrum has multiple velocity components, and the 1665 MHz line is not visible.

3.2.16. *IRAS 12018+1941*

This OHM was first found and reported by the Arecibo OHM surveys (Darling & Giovanelli 2002). The line profile and flux density observed by FAST are in good agreement with those of (Darling & Giovanelli 2002). The 1665 MHz line is clearly visible in the FAST observations, but not in (Darling & Giovanelli 2002). The measured line ratio is $R_{1667:1665} = 4.59 \pm 1.25$ (see Table 2). In Figure 20 the optical RGB image shows an apparent merging system with two extended tidal tails.

3.2.17. *IRAS 12232+5532*

The OHM IRAS 12232+5532 was first found and identified by the FASHI survey (see Figures 21). Its measured OH redshift is 0.23250, while the optically observed redshift is 0.23143 (Saunders et al. 2000) (see Tables 1 and 3). The velocity difference is only $\sim 150 \text{ km s}^{-1}$, and spatially the two are in good agreement. A careful search for other optical objects shows that there is no possible match to the radio observation. The optical RGB image shows an apparent merging system with tidal tails to the west and east of the nucleus. The OH spectrum shows several velocity components, probably indicating an active merging process. The velocity position of the 1665 MHz line shows a bright emission profile. The measured line ratio is $R_{1667:1665} = 1.54 \pm 0.18$.

3.2.18. *IRAS 12447+3721*

The OHM IRAS 12447+3721 was first found and identified by the FASHI survey (see Figures 22). Its measured OH redshift is 0.15847, which is in good agreement with the optically observed redshift of 0.15870 (Saunders et al. 2000) (see Tables 1 and 3). Moreover, the two are in good spatial agreement. A careful search for other optical objects shows that there is no possible match to the radio observation. The optical RGB image shows an apparent merging system with tidal tails to the west and east of the nucleus, or a spiral structure surrounding the nucleus. Duarte Puertas et al. (2017) classified it as a H II galaxy with a high star formation rate.

3.2.19. *IRAS 13070+6412*

The OHM IRAS 13070+6412 was first found and identified by the FASHI survey (see Figures 23). Its measured OH redshift is 0.20523, which is in good agreement with the optically observed redshift of 0.20492 (Saunders et al. 2000) (see Tables 1 and 3). Moreover, the two are in good spatial agreement. A careful search for other optical objects shows that there is no possible match to the radio observation. The optical RGB image shows a possible merging system with tidal tails to north and south of the nucleus. The OH spectrum is strong and has multiple velocity components, probably due to the merging interaction. There is a weak emission at 1665 MHz position, but it does not have enough SNR to be identified as a real signal.

3.2.20. *IRAS 13469+5833*

The OHM IRAS 13469+5833 was first found and identified by the FASHI survey (see Figures 24). Its measured OH redshift is 0.15716, while the optically observed redshift is 0.15778 (Saunders et al. 2000) (see Tables 1 and 3). The difference between the two is $\sim 350 \text{ km s}^{-1}$, but the two are in good spatial agreement. A careful search for other optical objects shows that there is no possible match to the radio observation. The optical RGB image shows a possible merging system with several tidal tails surrounding the nuclei (see also the HST F814W-band images in Murata et al. 2017). The OH spectrum has double velocity components, probably indicating merging activity. The IRAS 13469+5833 is identified as an H II galaxy (Lin et al. 2018).

3.2.21. *IRAS 14170+4545*

The OHM IRAS 14170+4545 was first found and identified by the FASHI survey (see Figures 25). Its measured OH redshift is 0.15009, which is in good agreement with the optically observed redshift of 0.15026 (Saunders et al. 2000) (see Tables 1 and 3). Moreover, the two are in good spatial agreement. A careful search for other optical objects shows that there is no possible match to the radio observation. The optical RGB image could not resolve the dense nucleus, but the extended materials show a possible tidal tail surrounding the nucleus. The OH spectrum has a very weak peak below $\sim 3.0 \text{ mJy}$, but the integrated flux shows a compact structure at the position of the OC.

3.2.22. *IRAS 14202+2615*

This source has been observed by the Arecibo OHM surveys (Darling & Giovanelli 2000, 2006), but they do not have sufficient sensitivity to see the OH emission

line. In the FASHI survey we detected the OHM emission line with a peak flux density of 4.38 ± 1.15 mJy, and the SNR is only about 3. The optical redshift from [Saunders et al. \(2000\)](#) is in good agreement with the OH line measured by FAST, while the spatially projected coordinate offset is $\sim 2.0'$. The optical RGB image shows two close nuclei, one of which has a visible tidal tail. This probably indicates a merging system.

3.2.23. IRAS 15043+5754

The OHM IRAS 15043+5754 was first found and identified by the FASHI survey (see Figures 27). Its measured OH redshift is 0.15029, which is in good agreement with the optically observed redshift of 0.15059 ([Saunders et al. 2000](#)) (see Tables 1 and 3). Moreover, the two are in good spatial agreement. A careful search for other optical objects shows that there is no possible match to the radio observation. The optical RGB image show a possible merging system with two nuclei interacting. The OH spectrum has a very weak peak below ~ 4.0 mJy, but the integrated flux shows a compact structure at the position of the optical object.

3.2.24. IRAS 15160+5307

The OHM IRAS 15160+5307 was first found and identified by the FASHI survey (see Figures 28). Its measured OH redshift is 0.15227, which is in good agreement with the optically observed redshift of 0.15199 ([Saunders et al. 2000](#)) (see Tables 1 and 3). Moreover, the two are in good spatial agreement. A careful search for other optical objects shows that there is no possible match to the radio observation. The optical RGB image shows a possible merging system with two interacting nuclei and at least two tidal tails. The OH spectrum has a weak peak of ~ 2.5 mJy, but the blue wing is broad and the red wing has an absorption feature.

3.2.25. IRAS 15261+5502

The new OHM IRAS 15261+5502 was first discovered by the FASHI survey (see Figures 29). The optical coordinates and spectroscopic redshift ($z_{\odot} = 0.22921$; [Abazajian et al. 2009](#)) are in good agreement with the observed OH line coordinates and redshift ($z_{\odot} = 0.22902$) for this object. The OH luminosity is $L_{\text{OH}} = 10^{3.43 \pm 0.01} L_{\odot}$ (see Table 1). It has a FIR luminosity of $L_{\text{FIR}} = 10^{11.99 \pm 0.03} L_{\odot}$ (see Table 3), which belongs to a LIRG. [Hou et al. \(2009\)](#) classified it as a starburst galaxy. In Figure 29 the optical RGB image shows two interacting nuclei with a visible tidal tail. The OH spectrum has a broad linewidth and multiple velocity components, probably resulting from a merger process.

3.2.26. IRAS 16468+5200

The new OHM IRAS 16468+5200 was first discovered by the FASHI survey (see Figures 30). The OH and the corresponding infrared parameters are listed in Tables 1 and 3. The optical coordinates and the spectroscopic redshift ($z_{\odot} = 0.15054$; [Saunders et al. 2000](#)) are in good agreement with the observed OH line coordinates and redshift ($z_{\odot} = 0.15032$) for this object. The OH luminosity is $L_{\text{OH}} = 10^{2.60 \pm 0.04} L_{\odot}$ (see Table 1). It has a FIR luminosity of $L_{\text{FIR}} = 10^{11.84 \pm 0.02} L_{\odot}$ (see Table 3), which belongs to a LIRG. [Weedman & Houck \(2008\)](#) classified it as a LINER-type active galaxy nucleus. In Figure 29 the optical RGB image shows a typical merging system with two interacting nuclei, one of which has an elongated tidal tail. The OH spectrum has multiple velocity components.

3.2.27. IRAS 23129+2548

This source has been confirmed as an OHM by the Arecibo OHM surveys ([Darling & Giovanelli 2001](#)). In the FAST observation the 1665 MHz line is not blind to the 1667 MHz line, but the 1665 MHz line shows no emission feature. The optical RGB image shows an interacting merging system with visible tidal tails. The nucleus of this OHM host is classified as a LINER by [Veilleux et al. \(1999\)](#). The OH spectrum has a broad linewidth and multiple velocity components, probably due to a merging process.

3.3. OHM catalog

Table 1 presents the main results of 27 OHMs detected by FASHI, including coordinate, redshift, line width, and flux. Each column in Table 1 is introduced as follows:

- Column 1: Index number for each FASHI extragalactic source. This index number is unique to each FASHI source.
- Column 2: Centroid coordinate (J2000) for the OH source in the format of Jhhmmss.ss±ddmmss.s.
- Column 3: IRAS source name ([Helou & Walker 1988](#)).
- Column 4-5: Right ascension (RA) and declination (DEC) in units of deg from the FASHI source centroid (J2000).
- Column 6: Redshift, z_{\odot} of the 1667 MHz OH line, corresponding to the heliocentric velocity in Column 6.
- Column 7: Heliocentric velocity of the H I source, cz_{\odot} in units of km s^{-1} . Values have been converted from the “radio” definition ($\delta\nu/\nu$) to the

Table 1. FASHI detected OHMs including coordinate, redshift, line width, peak flux.

[1]	[2]	[3]	[4]	[5]	[6]	[7]	[8]	[9]	[10]	[11]
FASHI ID	FASHI name	IRAS name	RA _{oh}	DEC _{oh}	z_{\odot}	V_{heli}	V_{CMB}	W_{50}	F_{peak}	rms
	J2000	B1950	deg	deg		km s ⁻¹	km s ⁻¹	km s ⁻¹	mJy	mJy
20240066172	J002814.52-015310.0	00256-0208	7.061	-1.886	0.27656	82912.1	82873.3	279.6	3.05	0.88
20240066090	J015902.56+254224.7	01562+2527	29.761	25.707	0.16600	49766.2	49727.5	272.8	6.72	1.43
20240066093	J025515.32+205835.5	02524+2046	43.814	20.977	0.18067	54164.0	54124.2	86.4	21.78	1.83
20240066181	J031336.48-023255.8	03111-0244	48.402	-2.549	0.18956	56827.9	56784.9	77.1	15.27	1.67
20240066097	J065143.27+220518.1	06487+2208	102.930	22.088	0.14347	43012.5	42973.8	130.4	5.82	1.37
20240066055	J082310.95+275137.6	08201+2801	125.796	27.860	0.16793	50343.5	50306.4	242.3	11.45	1.50
20240099047	J083634.98+513745.8	08328+5148	129.146	51.629	0.23749	71196.3	71161.8	105.9	10.63	1.10
20240066185	J085909.64-030430.6	08566-0252	134.790	-3.075	0.20262	60743.1	60702.9	190.2	7.73	1.27
20240066025	J101347.44+465356.6	10106+4708	153.448	46.899	0.20529	61543.0	61509.7	159.4	24.73	1.32
20240066062	J105837.38+382836.6	10558+3845	164.656	38.477	0.20788	62319.4	62286.1	26.3	4.35	1.04
20240066027	J110245.08+591005.0	10597+5926	165.688	59.168	0.19607	58780.0	58748.4	236.2	32.27	2.23
20240066060	J110537.56+311427.4	11029+3130	166.407	31.241	0.19885	59613.8	59579.5	130.2	3.36	0.97
20240066028	J111136.57+533514.0	11087+5351	167.902	53.587	0.14314	42913.0	42881.3	101.9	3.65	0.87
20240129741	J111908.12+600432.5	11161+6020	169.784	60.076	0.26434	79246.5	79215.1	288.2	9.07	2.05
20240066187	J113239.21-053833.9	11301-0523	173.163	-5.643	0.22984	68903.1	68862.2	168.0	6.98	1.46
20240066105	J120420.53+192456.7	12018+1941	181.086	19.416	0.16783	50315.5	50278.4	254.6	1.90	0.83
20240066030	J122539.49+551528.9	12232+5532	186.415	55.258	0.23250	69702.5	69672.8	166.1	2.40	0.66
20240066069	J124709.66+370508.6	12447+3721	191.790	37.086	0.15847	47506.6	47478.6	198.0	1.40	0.68
20240066013	J130854.87+635636.6	13070+6412	197.229	63.944	0.20523	61525.8	61496.1	154.6	12.48	1.97
20240066035	J134841.23+581817.8	13469+5833	207.172	58.305	0.15716	47114.4	47085.9	20.6	9.43	1.26
20240066034	J141859.45+453206.3	14170+4545	214.748	45.535	0.15009	44997.1	44970.9	68.7	2.43	0.85
20240066110	J142227.98+260225.7	14202+2615	215.617	26.040	0.15925	47740.6	47718.6	16.0	4.38	1.15
20240066037	J150535.42+574248.3	15043+5754	226.398	57.713	0.15029	45054.5	45026.5	115.9	2.17	1.16
20240066039	J151732.61+525616.8	15160+5307	229.386	52.938	0.15227	45648.2	45620.9	195.3	1.34	0.51
20240102609	J152725.70+545139.2	15261+5502	231.857	54.861	0.22902	68657.8	68630.3	218.0	8.42	1.04
20240066042	J164800.26+515535.2	16468+5200	252.001	51.926	0.15032	45065.1	45037.3	151.3	3.98	1.28
20240066122	J231519.36+260419.1	23129+2548	348.831	26.072	0.17881	53605.7	53570.5	278.4	3.42	0.96

Notes. The IRAS names in bold are previously known OHMs, while the others are first discovered by FAST.

optical definition $\delta\lambda/\lambda$. All results are presented in this work using the optical helio-centric definition of velocity.

- Column 8: Cosmic microwave background (CMB) rest-frame velocity. This is calculated from the heliocentric velocity using the solar motion with respect to the CMB as measured by [Fixsen et al. \(1996\)](#) with $v_{\odot} = 371 \pm 1 \text{ km s}^{-1}$ to $(l, b) = (264^{\circ}14 \pm 0^{\circ}15, 48^{\circ}26 \pm 0^{\circ}15)$.
- Column 9: Velocity width of the OH line profile, W_{50} in km s^{-1} , measured at the 50% level of each peak.
- Column 10: OH line peak intensity, F_{peak} in mJy.

- Column 11: OH line noise level for the spatially integrated spectral profile, σ_{rms} in mJy. It was obtained by measuring over the signal and RFI free portions of the integrated HI spectrum at a spectral resolution of 6.4 km s^{-1} .

3.4. Hyperfine ratio catalog

Table 2 presents the integrated flux and the hyperfine ratio between the 1667 and 1665 MHz lines. Each column in Table 2 is introduced as follows:

- Column 1: Index number for each FASHI extragalactic source. This index number is unique to each FASHI source.
- Column 2: IRAS source name ([Helou & Walker 1988](#)).

Table 2. Hyperfine ratio between the 1667 and 1665 MHz lines.

[1] FASHI ID	[2] IRAS name	[3] S_{int}^{1667} mJy·km s ⁻¹	[4] V_{min}^{1667} km s ⁻¹	[5] V_{max}^{1667} km s ⁻¹	[6] S_{int}^{1665} mJy·km s ⁻¹	[7] V_{min}^{1665} km s ⁻¹	[8] V_{max}^{1665} km s ⁻¹	[9] $R_{1667:1665}$ ratio
20240066172	00256-0208	1089.2 ± 65.1	82246.2	83457.0				
20240066090	01562+2527	2026.8 ± 93.5	49363.3	50148.7				
20240066093	02524+2046	1781.4 ± 59.1	54028.3	54243.2	607.3 ± 42.6	54481.4	54812.4	2.93 ± 0.23
20240066181	03111-0244	1167.6 ± 54.0	56703.8	56921.8	424.2 ± 57.8	57147.9	57600.9	2.75 ± 0.40
20240066097	06487+2208	848.0 ± 58.9	42839.9	43178.3	259.7 ± 46.8	43272.0	43524.6	3.27 ± 0.63
20240066055	08201+2801	2110.0 ± 77.8	50065.3	50568.3				
20240099047	08328+5148	1325.4 ± 50.6	70921.6	71376.2	140.4 ± 27.1	71578.6	71755.9	9.44 ± 1.85
20240066185	08566-0252	1427.1 ± 51.1	60584.7	60919.2				
20240066025	10106+4708	4011.7 ± 68.5	61332.6	61876.2				
20240066062	10558+3845	212.3 ± 46.7	62083.1	62492.4	130.7 ± 30.6	62604.4	62845.9	1.62 ± 0.52
20240066027	10597+5926	7259.4 ± 112.5	58535.6	59039.4	477.0 ± 45.2	59110.0	59489.0	15.22 ± 1.46
20240066060	11029+3130	424.8 ± 40.6	59463.6	59819.7				
20240066028	11087+5351	289.4 ± 27.2	42818.6	43005.8	219.1 ± 28.2	43200.4	43438.6	1.32 ± 0.21
20240129741	11161+6020	2468.3 ± 114.1	78901.6	79578.7				
20240066187	11301-0523	1014.8 ± 66.7	68669.5	69110.5				
20240066105	12018+1941	370.6 ± 37.4	50139.7	50530.3	80.8 ± 20.5	50688.3	50823.8	4.59 ± 1.25
20240066030	12232+5532	399.8 ± 26.0	69534.9	69869.2	259.2 ± 25.2	69969.6	70287.9	1.54 ± 0.18
20240066069	12447+3721	287.8 ± 33.0	47306.6	47749.7				
20240066013	13070+6412	2016.0 ± 91.6	61324.5	61764.1				
20240066035	13469+5833	556.0 ± 51.5	46975.8	47292.6				
20240066034	14170+4545	197.8 ± 36.1	44860.1	45194.9				
20240066110	14202+2615	319.4 ± 49.4	47601.5	47949.1				
20240066037	15043+5754	211.0 ± 44.5	44925.3	45202.0				
20240066039	15160+5307	305.5 ± 28.4	45368.5	45923.7				
20240102609	15261+5502	1857.3 ± 57.5	68312.8	68944.2				
20240066042	16468+5200	640.3 ± 57.8	44889.0	45267.6				
20240066122	23129+2548	845.4 ± 57.8	53272.0	53960.7				

Notes. The IRAS names in bold are previously known OHMs, while the others are first discovered by FAST.

- Column 3: Integrated flux of the 1667 MHz line, S_{int} , in mJy beam⁻¹km s⁻¹, by summing all velocity channels containing signal within an appropriate velocity range from each integrated spectrum. The velocity range is listed in Columns 3 and 4.
- Columns 4-5: The minimum (V_{min}^{1667}) and maximum (V_{max}^{1667}) of the integrated flux range for the 1667 MHz line.
- Column 6: Integrated flux of the 1665 MHz line, S_{int} , in mJy beam⁻¹km s⁻¹, by summing all velocity channels containing signal within an appropriate velocity range from each integrated spectrum. The velocity range is listed in Columns 6 and 7.

- Columns 7-8: The minimum (V_{min}^{1665}) and maximum (V_{max}^{1665}) of the integrated flux range for the 1665 MHz line.
- Column 9: Hyperfine line ratio between the 1667 and 1665 MHz lines.

3.5. OHM optical counterpart catalog

Table 3 presents the main results of the OCs corresponding to the OHMs, including WISE magnitude, IRAS flux, and FIR properties. Each column in Table 3 is introduced as follows:

- Column 1: Index number for each FASHI extragalactic source. This index number is unique to each FASHI source.
- Column 2: IRAS source catalog name.

Table 3. OHM optical counterparts including IRAS flux and FIR properties.

[1]	[2]	[3]	[4]	[5]	[6]	[7]	[8]	[9]	[10]
FASHI ID	IRAS name	RA _{oc}	DEC _{oc}	z_{\odot}	f_{60}	f_{100}	D_L	$\log L_{\text{FIR}}$	$\log L_{\text{OH}}$
	B1950	deg	deg	PSCz	Jy	Jy	$h_{75}^{-1} \text{Gpc}$	$h_{75}^{-2} L_{\odot}$	$h_{75}^{-2} L_{\odot}$
20240066172	00256-0208	7.059	-1.863	0.27630	0.65 ± 0.07	1.00 ± 0.00	1.258	12.22 ± 0.03	3.36 ± 0.03
20240066090	01562+2527	29.761	25.710	0.16580	0.80 ± 0.06	1.85 ± 0.15	0.718	11.90 ± 0.02	3.18 ± 0.02
20240066093	02524+2046	43.821	20.983	0.18153	0.94 ± 0.08	8.48 ± 0.00	0.787	12.43 ± 0.01	3.20 ± 0.01
20240066181	03111-0244	48.422	-2.560	0.18833	0.69 ± 0.06	1.03 ± 0.00	0.829	11.88 ± 0.02	3.06 ± 0.02
20240066097	06487+2208	102.941	22.074	0.14370	2.07 ± 0.17	2.36 ± 0.26	0.614	12.06 ± 0.03	2.68 ± 0.03
20240066055	08201+2801	125.803	27.861	0.16750	1.13 ± 0.09	1.60 ± 0.18	0.727	11.98 ± 0.03	3.21 ± 0.02
20240099047	08328+5148	129.150	51.627	0.23700	0.37 ± 0.11	1.58 ± 0.00	1.061	12.05 ± 0.05	3.31 ± 0.02
20240066185	08566-0252	134.789	-3.070	0.20201	0.79 ± 0.07	1.10 ± 0.00	0.891	11.99 ± 0.03	3.21 ± 0.02
20240066025	10106+4708	153.450	46.900	0.20481	0.77 ± 0.08	1.37 ± 0.30	0.904	12.04 ± 0.05	3.67 ± 0.01
20240066062	10558+3845	164.664	38.485	0.20660	0.70 ± 0.06	1.00 ± 0.00	0.917	11.97 ± 0.02	2.40 ± 0.10
20240066027	10597+5926	165.696	59.177	0.19583	1.02 ± 0.08	1.33 ± 0.17	0.860	12.06 ± 0.03	3.88 ± 0.01
20240066060	11029+3130	166.406	31.242	0.19890	1.04 ± 0.09	1.38 ± 0.11	0.873	12.09 ± 0.03	2.66 ± 0.04
20240066028	11087+5351	167.902	53.583	0.14270	1.00 ± 0.11	1.00 ± 0.13	0.613	11.73 ± 0.04	2.21 ± 0.04
20240129741	11161+6020	169.779	60.075	0.26428	0.61 ± 0.05	1.28 ± 0.19	1.196	12.21 ± 0.04	3.68 ± 0.02
20240066187	11301-0523	173.175	-5.663	0.23019	0.70 ± 0.07	1.42 ± 0.16	1.024	12.13 ± 0.03	3.17 ± 0.03
20240066105	12018+1941	181.102	19.419	0.16865	1.64 ± 0.18	1.86 ± 0.22	0.727	12.10 ± 0.04	2.46 ± 0.04
20240066030	12232+5532	186.410	55.264	0.23143	0.62 ± 0.06	1.63 ± 0.00	1.037	12.14 ± 0.02	2.77 ± 0.03
20240066069	12447+3721	191.782	37.094	0.15870	1.11 ± 0.12	1.00 ± 0.00	0.683	11.85 ± 0.04	2.30 ± 0.05
20240066013	13070+6412	197.231	63.941	0.20492	0.74 ± 0.05	0.71 ± 0.11	0.904	11.93 ± 0.03	3.37 ± 0.02
20240066035	13469+5833	207.167	58.315	0.15778	1.34 ± 0.11	1.99 ± 0.14	0.677	12.00 ± 0.02	2.58 ± 0.04
20240066034	14170+4545	214.745	45.537	0.15026	0.73 ± 0.06	1.19 ± 0.12	0.645	11.70 ± 0.03	2.09 ± 0.08
20240066110	14202+2615	215.631	26.035	0.15915	1.45 ± 0.16	1.95 ± 0.23	0.687	12.03 ± 0.04	2.35 ± 0.07
20240066037	15043+5754	226.415	57.719	0.15059	0.99 ± 0.07	1.42 ± 0.10	0.645	11.82 ± 0.02	2.12 ± 0.09
20240066039	15160+5307	229.374	52.947	0.15199	0.64 ± 0.03	1.38 ± 0.08	0.655	11.71 ± 0.02	2.29 ± 0.04
20240102609	15261+5502	231.861	54.864	0.22921	0.53 ± 0.05	1.00 ± 0.00	1.020	11.99 ± 0.03	3.43 ± 0.01
20240066042	16468+5200	252.006	51.929	0.15054	1.01 ± 0.07	1.61 ± 0.00	0.646	11.84 ± 0.02	2.60 ± 0.04
20240066122	23129+2548	348.839	26.076	0.17810	1.80 ± 0.20	1.70 ± 0.17	0.778	12.18 ± 0.04	2.87 ± 0.03

Notes. The IRAS names in bold are previously known OHMs, while the others are first discovered by FAST.

- Column 3-4: RA and DEC with centroid coordinate (J2000) in units deg for OHM OCs extracted from the SDSS catalog.
- Column 5: Heliocentric optical redshift, z_{\odot} , extracted from the SDSS catalog.
- Column 6-9: WISE 3.4, 4.6, 12, and $22 \mu\text{m}$ Vega magnitudes extracted from the unwise catalog.
- column 10-11: IRAS 60 and $100 \mu\text{m}$ flux densities f_{60} and f_{100} in units of Jy (Helou & Walker 1988).
- Column 12: Luminosity distance D_L in $h_{75}^{-1} \text{Gpc}$, estimated using the following equation from Darling & Giovanelli (2000) with

$$D_L = (V_{\text{CMB}}/H_0)(1 + 0.5z_{\text{CMB}}), \quad (1)$$

where V_{CMB} , listed in Table 1, is the radial velocity of the source in the cosmic microwave background (CMB) rest frame.

- Column 12: Logarithm of the FIR luminosity L_{FIR} in units of $h_{75}^{-2} L_{\odot}$, estimated using the following equation from Sanders & Mirabel (1996) with

$$L_{\text{FIR}} = 3.96 \times 10^5 D_L^2 (2.58 f_{60} + f_{100}), \quad (2)$$

where f_{60} and f_{100} are listed in Columns 9-10.

- Column 13: OH line luminosity L_{OH} in units of $h_{75}^{-2} L_{\odot}$. From the integrated line flux S_{int} we use the general relation for the spectral line luminosity (e.g., Briggs 1998) with

$$\frac{L_{\text{OH}}}{L_{\odot}} = \left(\frac{1.7064}{1 + z_{\text{OH}}} \right) \left(\frac{S_{\text{int}}}{\text{mJy km s}^{-1}} \right) \left(\frac{D_L}{\text{Gpc}} \right)^2, \quad (3)$$

where we take the stronger of the two main OH lines with a rest frequency of 1667.35903 MHz to define z_{OH} .

3.6. OHM catalog corss-matching with GSWLC

Table 4 shows the cross-matched 28 sources between all known 154 OHMs and the entire GSWLC catalog (Salim et al. 2007) under the condition $\delta_{\text{RA}} \leq 3'$, $\delta_{\text{DEC}} \leq 3'$ and $\delta_{\text{HI velocity}} \leq 300 \text{ km s}^{-1}$. Nine OHMs are detected by FAST. Each column in Table 3 is introduced as follows:

- Column 1: IRAS source catalog name.
- Column 2: OBJID, SDSS photometric identification number, from GSWLC.
- Column 3-4: RA and DEC with centroid coordinate (J2000) in units deg, from GSWLC.
- Column 5: Redshift, z_{\odot} , from GSWLC.
- Column 6: Stellar mass, $\log(M_{\star})$ with its error, from GSWLC.
- Column 7: UV/optical (SED) star formation rate, $\log(\text{SFR}_{\text{SED}})$ with its error, from GSWLC.
- Column 8: Dust attenuation, A_V , in rest-frame V , from GSWLC.

4. DISCUSSION

4.1. Hyperfine ratio

The 1667 and 1665 MHz lines refer to the main lines of OH at the radio rest frequencies of 1667.359 and 1665.402 MHz, while two satellite lines are located at 1720.530 and 1612.231 MHz (Radford 1964). In local thermodynamic equilibrium (LTE), the OH line ratios are approximately 1:5:9:1 for 1612, 1665, 1667, and 1720 MHz lines (Henkel et al. 1991; Hess et al. 2021). The 1667 MHz line is relatively common in extragalactic observations, but the 1665 MHz line is very rare because of its weakness. McBride et al. (2013) reported that the hyperfine line ratio is $1 < R_{1667:1665} < 10$ with an average of $R_{1667:1665} \approx 5$. In previous observations (e.g., Darling & Giovanelli 2000, 2001, 2002), the 1667 and 1665 MHz lines often blend into each other, resulting in a barely measurable line ratio. The main reason for this is the inherently large line width ($> 500 \text{ km s}^{-1}$) of the 1667 MHz line. In Table 2 we present the hyperfine line ratio between the integrated fluxes of 1667 and 1665 MHz. Totally we have detected 27 OHMs, 9 of which show a visible 1665 MHz line. The detection rate is 33.3% for the 1665 MHz line. The line ratio

$R_{1667:1665}$ ranges from 1.32 to 15.22, with an average of $R_{1667:1665} = 4.74$, in agreement with the results reported by McBride et al. (2013). Although the hyperfine ratio is often consistent with the thermal emission condition (Baan et al. 1982), e.g. for IRAS 10558+3845 with $R_{1667:1665} = 1.62 \pm 0.52$, 11087+5351 with $R_{1667:1665} = 1.32 \pm 0.21$, and 12232+5532 with $R_{1667:1665} = 1.54 \pm 0.18$, which have relatively low hyperfine ratios with $R_{1667:1665} < 2$, McBride et al. (2013) suggested that the OH emission probably includes a significant non-thermal contribution. Furthermore, the variable ratios with a wide range from 1.32 to 15.22 are indicative of complex maser pumping mechanisms.

4.2. Host galaxy properties

OHMs are predominantly found in the core of a class of galaxies called Luminous Infrared Galaxies (LIRGs) with $L_{\text{FIR}} > 10^{11} L_{\odot}$, and ultra-luminous infrared galaxies (ULIRGs) with FIR luminosities $L_{\text{FIR}} > 10^{12} L_{\odot}$ (e.g., Darling & Giovanelli 2002). In this work, 13 OHMs are ULIRGs and 14 OHMs are LIRGs based on the measured L_{FIR} , which ranges from $10^{11.70 \pm 0.03}$ to $10^{12.43 \pm 0.01} L_{\odot}$ with a median of $10^{12.00 \pm 0.02} L_{\odot}$. This means that all 27 OHMs have relatively high FIR luminosities. The strong FIR emission suggest that the host system has undergone a very recent and strong starburst (e.g., Sanders & Mirabel 1996).

The majority of [U]LIRGs or OHMs show evidence of interaction with other galaxies or have recently undergone a galaxy merger (Andreasian & Alloin 1994; Darling & Giovanelli 2002). Moreover, the hosts of [U]LIRGs are rich in molecular gas compared to spiral galaxies (Burdizuzha & Vikulov 1990). Mergers could be a way to funnel molecular gas into the core of the [U]LIRG, producing high molecular densities and stimulating the high star formation rates that are characteristic of [U]LIRGs. Pihlström (2007) suggested that the maser emission may originate in thick, circumnuclear structures, based on a general consensus with high-resolution imaging.

OHMs are likely a disturbed system in a galaxy merger, as evidenced by tidal tails (Clements et al. 1996). We found that almost all of the 27 OHMs have recently merged or interacted with another galaxy (see Figure 2 and the other figures in Appendix) and may be undergoing a burst of star formation. The detected OHMs have almost multiple velocity features, suggesting a velocity substructure throughout the detected regions. This could be an indication that this galaxy is in the process of merging as seen in the optical morphology (see Figure 2 and the other figures in Appendix). In general, OHM line emission is always detected in [U]LIRGs. It is

Table 4. Cross-matched sources between all the known 154 OHMs and GSWLC.

[1]	[2]	[3]	[4]	[5]	[6]	[7]	[8]
IRAS name	OBJID	RA	DEC	z_{\odot}	$\log(M_{\star})$	$\log(\text{SFR}_{\text{SED}})$	A_V
B1950		deg	deg		M_{\odot}	$M_{\odot} \text{ yr}^{-1}$	mag
0758+2851	1237657629506142647	119.727	28.886	0.1262	10.70 ± 0.03	-0.54 ± 0.71	0.24 ± 0.10
08122+0505	1237660668730408974	123.723	4.937	0.1033	11.04 ± 0.04	0.57 ± 0.24	0.43 ± 0.16
08449+2332	1237664834854518934	131.959	23.353	0.1517	10.71 ± 0.06	1.47 ± 0.05	0.47 ± 0.06
09039+0503	1237658423543595297	136.642	4.858	0.1250	10.81 ± 0.03	1.56 ± 0.06	0.86 ± 0.06
09116+0334	1237654605316358298	138.574	3.365	0.1460	10.91 ± 0.03	0.43 ± 0.16	0.23 ± 0.10
09320+6134	1237651272966275163	143.965	61.353	0.0394	11.25 ± 0.03	1.16 ± 0.01	0.75 ± 0.00
09531+1430	1237671261205495893	148.958	14.269	0.2152	11.34 ± 0.04	1.00 ± 0.18	0.62 ± 0.12
09540+3521	1237664669506863314	149.246	35.119	0.1006	10.72 ± 0.03	0.36 ± 0.23	0.59 ± 0.11
10378+1108	1237661949170155593	160.122	10.888	0.1363	11.03 ± 0.03	1.57 ± 0.02	0.82 ± 0.03
10558+3845	1237664668975562850	164.664	38.485	0.2081	11.01 ± 0.09	1.56 ± 0.14	0.69 ± 0.14
11011+4107	1237662194520293391	165.976	40.850	0.0348	9.97 ± 0.14	0.58 ± 0.18	0.49 ± 0.11
11087+5351	1237657590319022140	167.902	53.583	0.1429	10.91 ± 0.07	1.44 ± 0.20	0.73 ± 0.18
11257+5850	1237655107301277787	172.140	58.563	0.0105	10.40 ± 0.04	0.85 ± 0.08	0.86 ± 0.09
12018+1941	1237667914881892435	181.102	19.419	0.1679	10.89 ± 0.09	1.44 ± 0.12	0.60 ± 0.15
12447+3721	1237664672714653739	191.782	37.094	0.1582	10.39 ± 0.09	0.96 ± 0.18	0.24 ± 0.15
13254+4754	1237661149769760972	201.900	47.647	0.0607	9.77 ± 0.07	0.33 ± 0.08	0.17 ± 0.08
13428+5608	1237661387602853939	206.176	55.887	0.0373	10.77 ± 0.05	0.35 ± 0.33	0.39 ± 0.14
13469+5833	1237659326015537309	207.167	58.314	0.1575	11.00 ± 0.05	0.90 ± 0.14	0.40 ± 0.14
14202+2615	1237665441523957822	215.631	26.035	0.1587	11.05 ± 0.05	1.38 ± 0.02	0.20 ± 0.02
14312+2825	1237665351854784676	218.365	28.200	0.1748	11.30 ± 0.09	1.59 ± 0.05	0.73 ± 0.08
14488+3521	1237662305655717891	222.726	35.144	0.2057	11.41 ± 0.04	2.23 ± 0.02	0.73 ± 0.01
15043+5754	1237671769072206053	226.415	57.719	0.1506	10.67 ± 0.06	1.29 ± 0.10	0.44 ± 0.14
15160+5307	1237655463779631232	229.374	52.946	0.1522	11.21 ± 0.06	1.47 ± 0.08	0.37 ± 0.11
15224+1033	1237662636908478686	231.213	10.380	0.1346	10.78 ± 0.05	1.13 ± 0.05	0.34 ± 0.03
15250+3608	1237662335714852881	231.748	35.977	0.0552	10.63 ± 0.04	0.97 ± 0.06	0.38 ± 0.06
15327+2340	1237665537075511390	233.738	23.504	0.0184	10.87 ± 0.02	0.37 ± 0.08	0.69 ± 0.07
16145+4231	1237665356696846411	244.050	42.400	0.0232	9.76 ± 0.04	-0.33 ± 0.10	0.19 ± 0.09
16300+1558	1237665536008520057	248.089	15.863	0.2418	11.20 ± 0.09	1.71 ± 0.13	0.49 ± 0.15

Notes. The listed Columns [2]-[8] in this catalog are extracted from GSWLC (Salim et al. 2007).

likely that OHMs occur during a particular state or stage of the merger, which are consequences of tidal density enhancements that accompany galaxy interactions (Darling 2007; Pihlström 2007). In fact, very-long-baseline interferometry (VLBI) radio images of Arp220 show that the OHM emission arises in regions only a few parsecs in size in its core, and have been used to support active galactic nucleus (AGN) models for this galaxy (Skinner et al. 1997).

The multi-wavelength SED fitting results in Figure 3 also show that the OH host galaxies are massive ($M_{\star} \simeq 10^{11} M_{\odot}$) galaxies with the SFR above the star-forming main sequence. The higher A_V value of the OH galaxies from the SED fit is also consistent with the high IR luminosities. On the other hand, not all ULIRGs

have detectable OH emission, suggesting that the OH emission may be triggered within a specific stage of the merger. High-resolution OH mapping observations, e.g. with the Very Large Array (VLA), are still needed to better constrain the physical origin of the OH emission.

4.3. L_{OH} and L_{FIR} Relationship

An OHM is proposed as radiatively pumped by the FIR radiation field at 35 and 53 μm , and then masing could be stimulated by 18 cm continuum emission from the surrounding condition (Henkel et al. 1987). In a simple scenario of low-gain unsaturated masing, the maser power is proportional to the pumping rate and the stimulated emission rate (Baan 1989). If the observed OHM represents an ensemble of many indi-

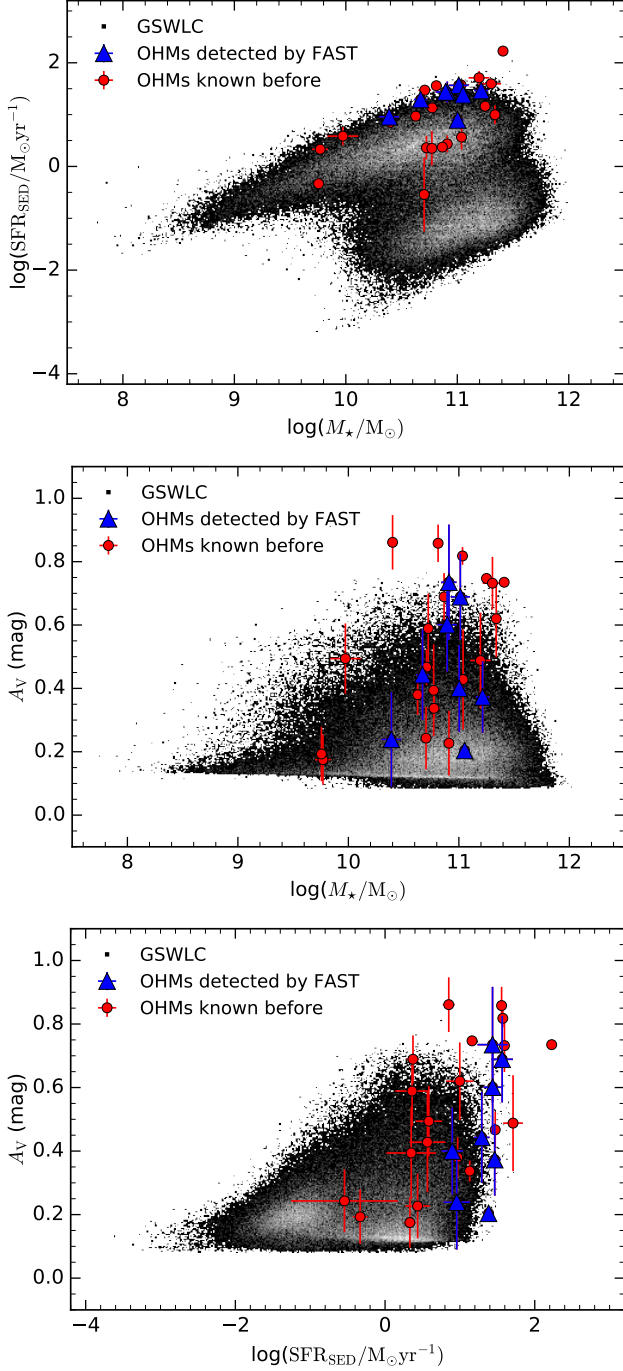


Figure 3. The distributions between $\log(M_*)$, $\log(\text{SFR}_{\text{SED}})$, and A_V . The background shows all the data in the GSWLC catalog. The red dots indicate the cross-matched 28 sources between all known 154 OHMs and the entire GSWLC catalog. The blue triangles indicate the cross-matched OHMs detected by FAST.

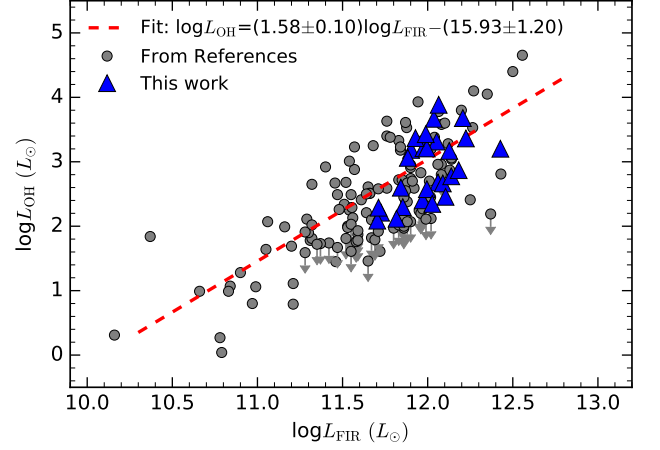


Figure 4. L_{OH} vs. L_{FIR} distribution including 154 sources. The blue triangles indicate five OHMs discovered by FASHI. The grey dots indicate the detection results of previously known OHMs (Darling & Giovanelli 2002, 2006; Willett 2012; Suess et al. 2016; Hess et al. 2021; Glowacki et al. 2022; Jarvis et al. 2023), where the sources with L_{OH} having only an upper limit are excluded from the current fitting statistics. The red dashed line shows the fitting result of the $L_{\text{OH}}-L_{\text{FIR}}$ relation.

vidual masing regions with different saturation states, then the relationship between OH and FIR luminosity is $L_{\text{OH}} \propto L_{\text{FIR}}^{1 < \gamma < 2}$ (Baan 1989; Darling & Giovanelli 2002; Yun et al. 2001). The measurement of γ has always been frustrated by small samples, survey bias, and theoretical bias. Darling & Giovanelli (2002) derived the relationship between OH and far IR luminosity with 95 data points as $\log L_{\text{OH}} = (1.57 \pm 0.11) \log L_{\text{FIR}} - (15.76 \pm 1.22)$. In this work we detect 27 OHMs and 18 new OHMs, plus 127 other previously known OHMs with OH and FIR luminosities from the literature (Darling & Giovanelli 2002, 2006; Willett 2012; Suess et al. 2016; Hess et al. 2021; Glowacki et al. 2022), where 31 sources with L_{OH} having only an upper limit are excluded from the current fitting statistics. Using the least-squares fitting method, the samples produce a fitting result with $\log L_{\text{OH}} = (1.58 \pm 0.10) \log L_{\text{FIR}} - (15.93 \pm 1.20)$ in Figure 4. The $\gamma = 1.58 \pm 0.10$ agrees well with the result of Darling & Giovanelli (2002) with $\gamma = 1.57 \pm 0.11$. Therefore, γ remains almost the same when the OHM samples reach up to 154, which is ~ 1.6 times the previously known OHMs.

4.4. FAST OHM detectability

Currently, the highest redshift detection of such an OHM in the main 1667 MHz OH emission line is J095903.22+025356.1 with a redshift of $z_{\text{OH}} = 0.7092$, recently found by Jarvis et al. (2023). The second highest is LADUMA J033046.20-275518.1 with a redshift of

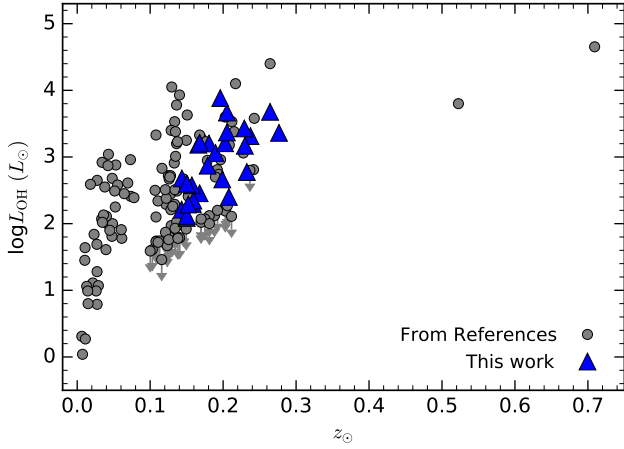


Figure 5. L_{OH} vs. z_{OH} distribution including 154 sources. The blue triangles indicate 18 new found OHMs by FASHI and . The grey dots indicate the detection results of previously known OHMs (Darling & Giovanelli 2002, 2006; Willett 2012; Suess et al. 2016; Hess et al. 2021; Glowacki et al. 2022; Jarvis et al. 2023). Each grey dot with a down arrow indicates the source with L_{OH} having only an upper limit.

$z_{\text{OH}} = 0.5225$, found by Glowacki et al. (2022). However, the third highest redshift of OHMs is IRAS 00256-0208 with $z_{\text{OH}} = 0.27656$, found in this paper. The large gap (see Figure 5) between the three highest redshifts of OHMs requires more new observatories to complete the OHM picture. The 19-beam receiver with FAST is capable of simultaneously covering a frequency range of 1000-1500 MHz, and the Ultra-Wide Bandwidth (UWB) receiver with FAST could simultaneously cover 500-3300 MHz. FAST will be a powerful instrument for observing highly redshifted OH emission in extragalactic objects (Zhang et al. 2023).

Furthermore, radio frequency interference (RFI) always affects the search results of astronomical observations for all radio telescopes on Earth. At present, the redshifts of all known OHMs are mainly below $z \approx 0.27$ or $f \approx 1310$ MHz (Darling & Giovanelli 2002; Willett 2012; Haynes et al. 2018; Suess et al. 2016; Hess et al. 2021; Roberts et al. 2021), which is mainly due to the existence of strong RFI above $z \approx 0.27$. From the statistics of RFI in the FAST 19-beam array (Zhang et al. 2023), we can see that there is a lot of seriously strong RFI from communication and navigation satellites, over two broad frequency bands in 1150-1310 and 1465-1500 MHz, corresponding to a redshift of $0.27 \lesssim z \lesssim 0.45$ and $0.11 \lesssim z \lesssim 0.14$, respectively. It is because the frequency band in 1310-1465 MHz is very clear that the FAST has already detected 27 OHMs in this band. In addition, the RFI is bearable in the frequency band of 1050-1150 MHz or $0.45 \lesssim z \lesssim 0.55$. Therefore, it is feasible to search for

the potential OHMs within $0.45 \lesssim z \lesssim 0.55$ using the FASHI data in the future.

Moreover, the FASHI data have detected 27 OHMs in the frequency range 1310-1465 MHz with a typical spectral detection sensitivity of ~ 1.50 mJy at a spectral resolution of ~ 6.4 km s $^{-1}$ at 1.4 GHz (Zhang et al. 2024). The coverage of the current FASHI data is ~ 10000 deg 2 . If the FASHI observation could cover ~ 20000 deg 2 in the future, FASHI is expected to obtain a total of 54 OHMs at the current detection sensitivity. If a longer integrated time than the current FASHI drift survey is applied to each PSCz source, more OHMs would be extracted. Please note that the method of source identification in this work is to directly compare the PSCz catalog with the corresponding FASHI data cube to see if there are any emission lines (see Section 2.2). A blind and complete OHM identification throughout the FASHI data cube would expand the sample again. Thus, FASHI or FAST could provide great opportunities to detect more samples.

5. SUMMARY

The **FAST All Sky H I** survey (FASHI) aims to cover the entire sky observable by the Five-hundred-meter Aperture Spherical radio Telescope (FAST), covering ~ 22000 square degrees of declination between -14° and $+66^\circ$, and in the frequency range of 1000-1500 MHz, with an expectation of detecting more than 100000 H I sources finally. At present, FASHI had observed more than 7600 square degrees. It has a typical spectral detection sensitivity of ~ 1.50 mJy and a spectral line velocity resolution of ~ 6.4 km s $^{-1}$ at a frequency of ~ 1.4 GHz. As of now, a total of 41741 extragalactic H I sources have been detected and released by FASHI.

To efficiently expand the OHM sample, we have directly cross-checked the PSCz catalog with the corresponding FASHI data cube. We finally detected 27 OHMs including 9 previously known and 18 new ones within a redshift range of $0.14314 \lesssim z_{\text{OH}} \lesssim 0.27656$. For 9 of the detected 27 OHMs, we also measured the hyperfine line ratio between the integrated fluxes of 1667 and 1665 MHz. The detection rate is 33.3% for the 1665 MHz line. The line ratio $R_{1667:1665}$ ranges from 1.32 to 15.22, with an average of $R_{1667:1665} = 4.74$, in agreement with the results reported by McBride et al. (2013).

Now we have a total of 154 OHMs, including the 18 OHMs first detected by FASHI. All samples produce a new fitting L_{OH} and L_{FIR} relationship with $\log L_{\text{OH}} = (1.58 \pm 0.10) \log L_{\text{FIR}} - (15.93 \pm 1.20)$, which agrees well with the result of Darling & Giovanelli (2002) with $\gamma = 1.57 \pm 0.11$ with 95 data points. This indicates that γ

remains almost the same when the OHM samples reach up to ~ 1.6 times the previously known OHMs.

In the detected 27 OHMs of this work, 13 OHMs are ULIRGs and 14 OHMs are LIRGs, ranging from $10^{11.70 \pm 0.03}$ to $10^{12.43 \pm 0.01} L_{\odot}$ with a median of $10^{12.00 \pm 0.02} L_{\odot}$. This means that all 27 OHMs have relatively high FIR luminosities. The strong FIR emission suggest that the host system has undergone a very recent and strong starburst. The multi-wavelength SED fitting results also show that the OH host galaxies are massive ($M_{*} \simeq 10^{11} M_{\odot}$) galaxies with the SFR above the star-forming main sequence. The higher A_V value of the OH galaxies from the SED fit is also consistent with the high IR luminosities. On the other hand, not all ULIRGs have detectable OH emission, suggesting that the OH emission may be triggered within a specific stage of the merger.

FAST, with its 19-beam array and UWB receiver, will be a powerful tool for observing more OHMs and unraveling their mystery in the future.

ACKNOWLEDGEMENTS

This work is supported by the National Key R&D Program of China (2022YFA1602901). CPZ acknowledges support by the West Light Foundation of the Chinese Academy of Sciences (CAS). CC is supported by the National Natural Science Foundation of China, Nos. 11803044, 11933003, and 12173045. This work is sponsored (in part) by the Chinese Academy of Sciences (CAS), through a grant to the CAS South America Center for Astronomy (CASSACA). We acknowledge the science research grants from the China Manned Space Project with No. CMS-CSST-2021-A05. We also wish

to thank the anonymous referee for comments that improved the clarity of the paper.

FAST is a Chinese national mega-science facility, operated by the National Astronomical Observatories of Chinese Academy of Sciences (NAOC). SDSS acknowledges support and resources from the Center for High-Performance Computing at the University of Utah. The SDSS web site is www.sdss4.org. SDSS is managed by the Astrophysical Research Consortium for the Participating Institutions of the SDSS Collaboration including the Brazilian Participation Group, the Carnegie Institution for Science, Carnegie Mellon University, Center for Astrophysics — Harvard & Smithsonian (CfA), the Chilean Participation Group, the French Participation Group, Instituto de Astrofísica de Canarias, The Johns Hopkins University, Kavli Institute for the Physics and Mathematics of the Universe (IPMU) / University of Tokyo, the Korean Participation Group, Lawrence Berkeley National Laboratory, Leibniz Institut für Astrophysik Potsdam (AIP), Max-Planck-Institut für Astronomie (MPIA Heidelberg), Max-Planck-Institut für Astrophysik (MPA Garching), Max-Planck-Institut für Extraterrestrische Physik (MPE), National Astronomical Observatories of China, New Mexico State University, New York University, University of Notre Dame, Observatório Nacional / MCTI, The Ohio State University, Pennsylvania State University, Shanghai Astronomical Observatory, United Kingdom Participation Group, Universidad Nacional Autónoma de México, University of Arizona, University of Colorado Boulder, University of Oxford, University of Portsmouth, University of Utah, University of Virginia, University of Washington, University of Wisconsin, Vanderbilt University, and Yale University.

REFERENCES

- Abazajian, K. N., Adelman-McCarthy, J. K., Agüeros, M. A., et al. 2009, *ApJS*, 182, 543, doi: [10.1088/0067-0049/182/2/543](https://doi.org/10.1088/0067-0049/182/2/543)
- Alatalo, K., Cales, S. L., Rich, J. A., et al. 2016, *ApJS*, 224, 38, doi: [10.3847/0067-0049/224/2/38](https://doi.org/10.3847/0067-0049/224/2/38)
- Andreassian, N., & Alloin, D. 1994, *A&AS*, 107, 23
- Baan, W. A. 1989, *ApJ*, 338, 804, doi: [10.1086/167237](https://doi.org/10.1086/167237)
- Baan, W. A. 1991, in *Astronomical Society of the Pacific Conference Series*, Vol. 16, *Atoms, Ions and Molecules: New Results in Spectral Line Astrophysics*, ed. A. D. Haschick & P. T. P. Ho, 45
- Baan, W. A., Rhoads, J., Fisher, K., Altschuler, D. R., & Haschick, A. 1992, *ApJL*, 396, L99, doi: [10.1086/186526](https://doi.org/10.1086/186526)
- Baan, W. A., Wood, P. A. D., & Haschick, A. D. 1982, *ApJL*, 260, L49, doi: [10.1086/183868](https://doi.org/10.1086/183868)
- Briggs, F. H. 1998, *A&A*, 336, 815, doi: [10.48550/arXiv.astro-ph/9710143](https://doi.org/10.48550/arXiv.astro-ph/9710143)
- Burduzha, V. V., & Vikulov, K. A. 1990, *MNRAS*, 244, 86
- Clements, D. L., Sutherland, W. J., McMahon, R. G., & Saunders, W. 1996, *MNRAS*, 279, 477, doi: [10.1093/mnras/279.2.477](https://doi.org/10.1093/mnras/279.2.477)
- Darling, J. 2007, *ApJL*, 669, L9, doi: [10.1086/523756](https://doi.org/10.1086/523756)
- Darling, J., & Giovanelli, R. 2000, *AJ*, 119, 3003, doi: [10.1086/301403](https://doi.org/10.1086/301403)
- . 2001, *AJ*, 121, 1278, doi: [10.1086/319413](https://doi.org/10.1086/319413)
- . 2002, *AJ*, 124, 100, doi: [10.1086/341166](https://doi.org/10.1086/341166)
- . 2006, *AJ*, 132, 2596, doi: [10.1086/508513](https://doi.org/10.1086/508513)
- Duarte Puertas, S., Vilchez, J. M., Iglesias-Páramo, J., et al. 2017, *A&A*, 599, A71, doi: [10.1051/0004-6361/201629044](https://doi.org/10.1051/0004-6361/201629044)

- Fixsen, D. J., Cheng, E. S., Gales, J. M., et al. 1996, *ApJ*, 473, 576, doi: [10.1086/178173](https://doi.org/10.1086/178173)
- Giovanelli, R., & Haynes, M. P. 2015, *A&A Rv*, 24, 1, doi: [10.1007/s00159-015-0085-3](https://doi.org/10.1007/s00159-015-0085-3)
- Glowacki, M., Collier, J. D., Kazemi-Moridani, A., et al. 2022, *ApJL*, 931, L7, doi: [10.3847/2041-8213/ac63b0](https://doi.org/10.3847/2041-8213/ac63b0)
- Haynes, M. P., Giovanelli, R., Kent, B. R., et al. 2018, *ApJ*, 861, 49, doi: [10.3847/1538-4357/aac956](https://doi.org/10.3847/1538-4357/aac956)
- Helou, G., & Walker, D. W. 1988, 0, <https://www.osti.gov/biblio/6458812>
- Henkel, C., Baan, W. A., & Mauersberger, R. 1991, *A&A Rv*, 3, 47, doi: [10.1007/BF00873457](https://doi.org/10.1007/BF00873457)
- Henkel, C., Guesten, R., & Baan, W. A. 1987, *A&A*, 185, 14
- Hess, K. M., Roberts, H., Dénes, H., et al. 2021, *A&A*, 647, A193, doi: [10.1051/0004-6361/202040019](https://doi.org/10.1051/0004-6361/202040019)
- Hou, L. G., Wu, X.-B., & Han, J. L. 2009, *ApJ*, 704, 789, doi: [10.1088/0004-637X/704/1/789](https://doi.org/10.1088/0004-637X/704/1/789)
- Jarvis, M. J., Heywood, I., Jewell, S. M., et al. 2023, *arXiv e-prints*, arXiv:2312.04345, <https://arxiv.org/abs/2312.04345>
- Jiang, P., Yue, Y., Gan, H., et al. 2019, *Science China Physics, Mechanics, and Astronomy*, 62, 959502, doi: [10.1007/s11433-018-9376-1](https://doi.org/10.1007/s11433-018-9376-1)
- Jiang, P., Tang, N.-Y., Hou, L.-G., et al. 2020, *Research in Astronomy and Astrophysics*, 20, 064, doi: [10.1088/1674-4527/20/5/64](https://doi.org/10.1088/1674-4527/20/5/64)
- Kim, D. C., Veilleux, S., & Sanders, D. B. 1998, *ApJ*, 508, 627, doi: [10.1086/306409](https://doi.org/10.1086/306409)
- Lin, Y.-T., Huang, H.-J., & Chen, Y.-C. 2018, *AJ*, 155, 188, doi: [10.3847/1538-3881/aab5b4](https://doi.org/10.3847/1538-3881/aab5b4)
- Lo, K. Y. 2005, *ARA&A*, 43, 625, doi: [10.1146/annurev.astro.41.011802.094927](https://doi.org/10.1146/annurev.astro.41.011802.094927)
- Lockett, P., & Elitzur, M. 2008, *ApJ*, 677, 985, doi: [10.1086/533429](https://doi.org/10.1086/533429)
- McBride, J., Heiles, C., & Elitzur, M. 2013, *ApJ*, 774, 35, doi: [10.1088/0004-637X/774/1/35](https://doi.org/10.1088/0004-637X/774/1/35)
- Murata, K. L., Yamada, R., Oyabu, S., et al. 2017, *MNRAS*, 472, 39, doi: [10.1093/mnras/stx1902](https://doi.org/10.1093/mnras/stx1902)
- Nan, R., Li, D., Jin, C., et al. 2011, *International Journal of Modern Physics D*, 20, 989, doi: [10.1142/S0218271811019335](https://doi.org/10.1142/S0218271811019335)
- Nikutta, R., Hunt-Walker, N., Nenkova, M., Ivezić, Ž., & Elitzur, M. 2014, *MNRAS*, 442, 3361, doi: [10.1093/mnras/stu1087](https://doi.org/10.1093/mnras/stu1087)
- Osterbrock, D. E. 1989, *Astrophysics of gaseous nebulae and active galactic nuclei*
- Pihlström, Y. M. 2007, in *Astrophysical Masers and their Environments*, ed. J. M. Chapman & W. A. Baan, Vol. 242, 446–451, doi: [10.1017/S1743921307013579](https://doi.org/10.1017/S1743921307013579)
- Radford, H. E. 1964, *PhRvL*, 13, 534, doi: [10.1103/PhysRevLett.13.534](https://doi.org/10.1103/PhysRevLett.13.534)
- Roberts, H., Darling, J., & Baker, A. J. 2021, *ApJ*, 911, 38, doi: [10.3847/1538-4357/abe944](https://doi.org/10.3847/1538-4357/abe944)
- Salim, S., Rich, R. M., Charlot, S., et al. 2007, *ApJS*, 173, 267, doi: [10.1086/519218](https://doi.org/10.1086/519218)
- Sanders, D. B., & Mirabel, I. F. 1996, *ARA&A*, 34, 749, doi: [10.1146/annurev.astro.34.1.749](https://doi.org/10.1146/annurev.astro.34.1.749)
- Saunders, W., Sutherland, W. J., Maddox, S. J., et al. 2000, *MNRAS*, 317, 55, doi: [10.1046/j.1365-8711.2000.03528.x](https://doi.org/10.1046/j.1365-8711.2000.03528.x)
- Skinner, C. J., Smith, H. A., Sturm, E., et al. 1997, *Nature*, 386, 472, doi: [10.1038/386472a0](https://doi.org/10.1038/386472a0)
- Suess, K. A., Darling, J., Haynes, M. P., & Giovanelli, R. 2016, *MNRAS*, 459, 220, doi: [10.1093/mnras/stw666](https://doi.org/10.1093/mnras/stw666)
- Toba, Y., Oyabu, S., Matsuhara, H., et al. 2014, *ApJ*, 788, 45, doi: [10.1088/0004-637X/788/1/45](https://doi.org/10.1088/0004-637X/788/1/45)
- Veilleux, S., Kim, D. C., & Sanders, D. B. 1999, *ApJ*, 522, 113, doi: [10.1086/307634](https://doi.org/10.1086/307634)
- Veilleux, S., Kim, D. C., Sanders, D. B., Mazzarella, J. M., & Soifer, B. T. 1995, *ApJS*, 98, 171, doi: [10.1086/192158](https://doi.org/10.1086/192158)
- Weedman, D. W., & Houck, J. R. 2008, *ApJ*, 686, 127, doi: [10.1086/591123](https://doi.org/10.1086/591123)
- Wiggins, B. K., Migenes, V., & Smidt, J. M. 2016, *ApJ*, 816, 55, doi: [10.3847/0004-637X/816/2/55](https://doi.org/10.3847/0004-637X/816/2/55)
- Willett, K. W. 2012, in *Cosmic Masers - from OH to H₂O*, ed. R. S. Booth, W. H. T. Vlemmings, & E. M. L. Humphreys, Vol. 287, 345–349, doi: [10.1017/S1743921312007284](https://doi.org/10.1017/S1743921312007284)
- Yun, M. S., Reddy, N. A., & Condon, J. J. 2001, *ApJ*, 554, 803, doi: [10.1086/323145](https://doi.org/10.1086/323145)
- Zhang, C.-P., Jiang, P., Zhu, M., et al. 2023, *Research in Astronomy and Astrophysics*, 23, 075016, doi: [10.1088/1674-4527/acd58e](https://doi.org/10.1088/1674-4527/acd58e)
- Zhang, C.-P., Zhu, M., Jiang, P., et al. 2024, *SCPMA*, 67, 219511, doi: [10.1007/s11433-023-2219-7](https://doi.org/10.1007/s11433-023-2219-7)

APPENDIX

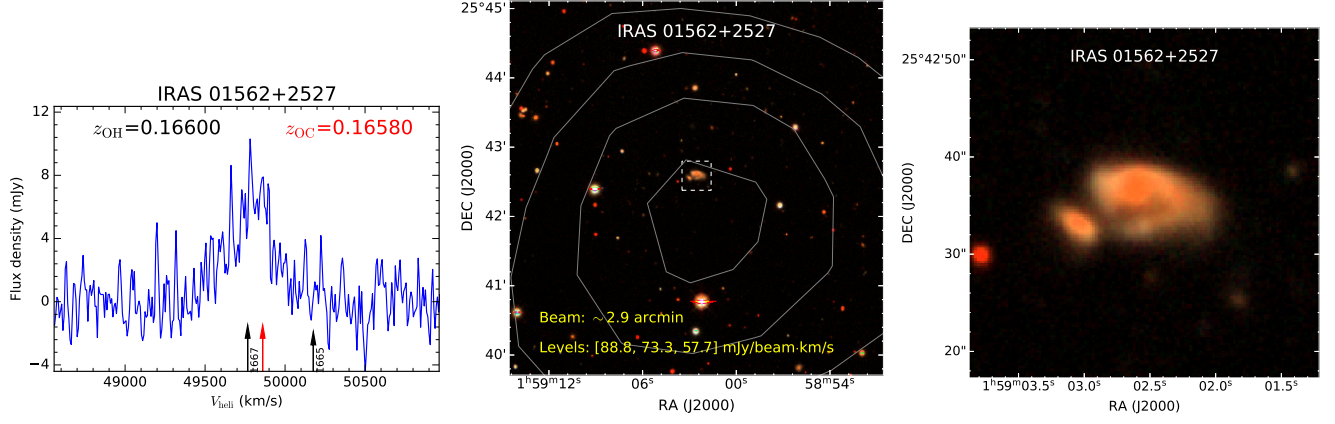


Figure 6. OHM IRAS 01562+2527. Refer to caption in Figure 2

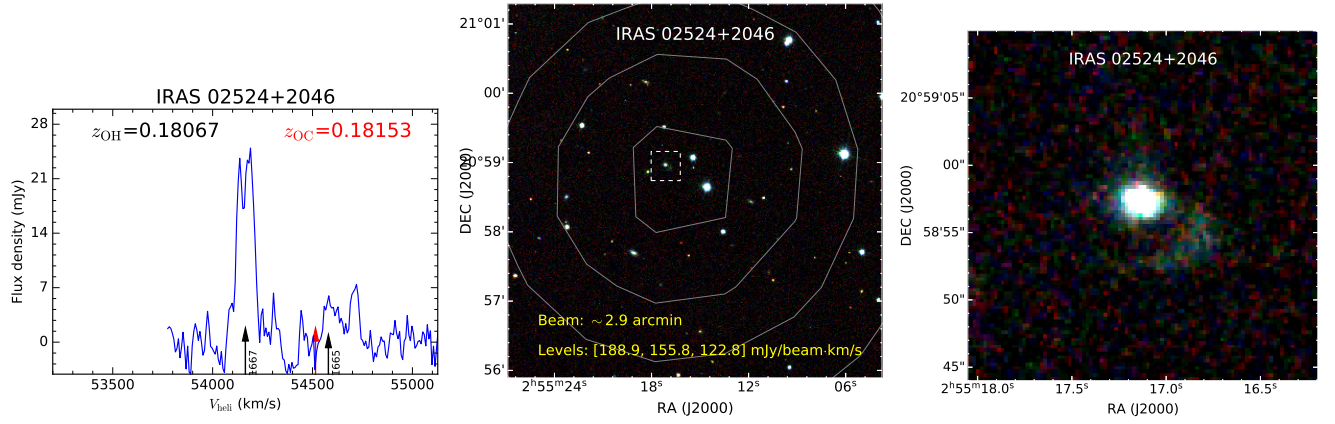


Figure 7. OHM IRAS 02524+2046. Refer to caption in Figure 2

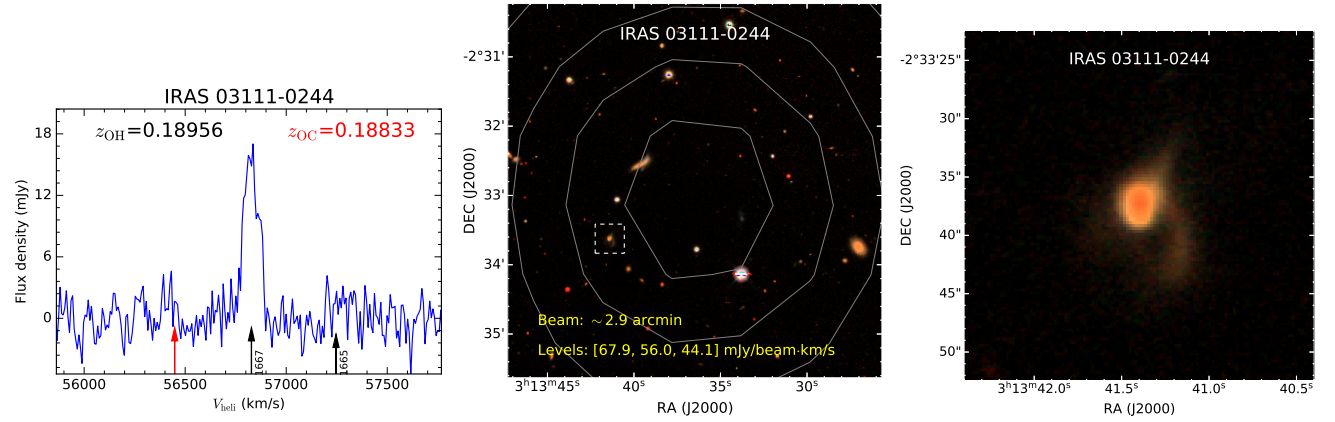


Figure 8. OHM IRAS 03111-0244. Refer to caption in Figure 2

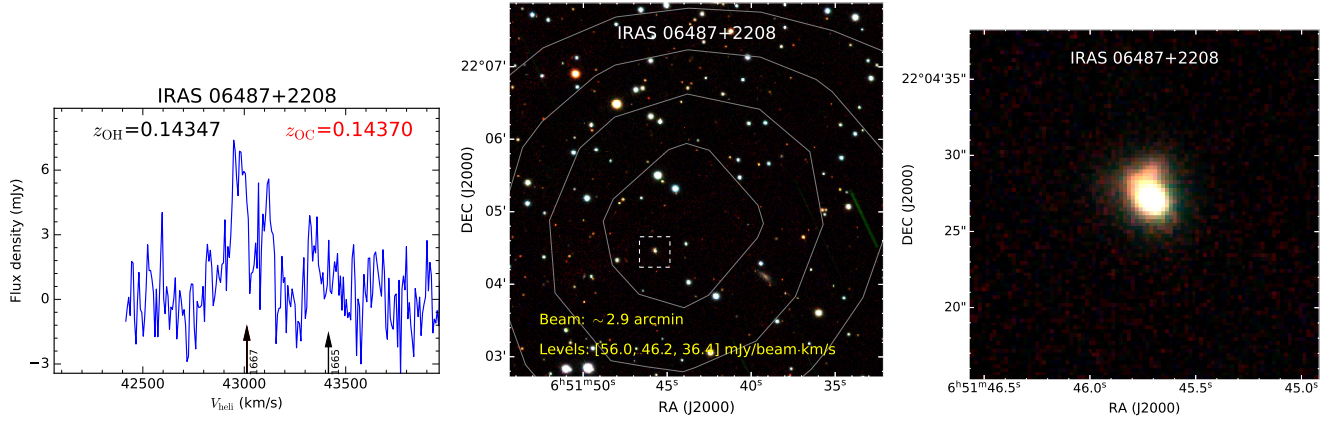


Figure 9. OHM IRAS 06487+2208. Refer to caption in Figure 2

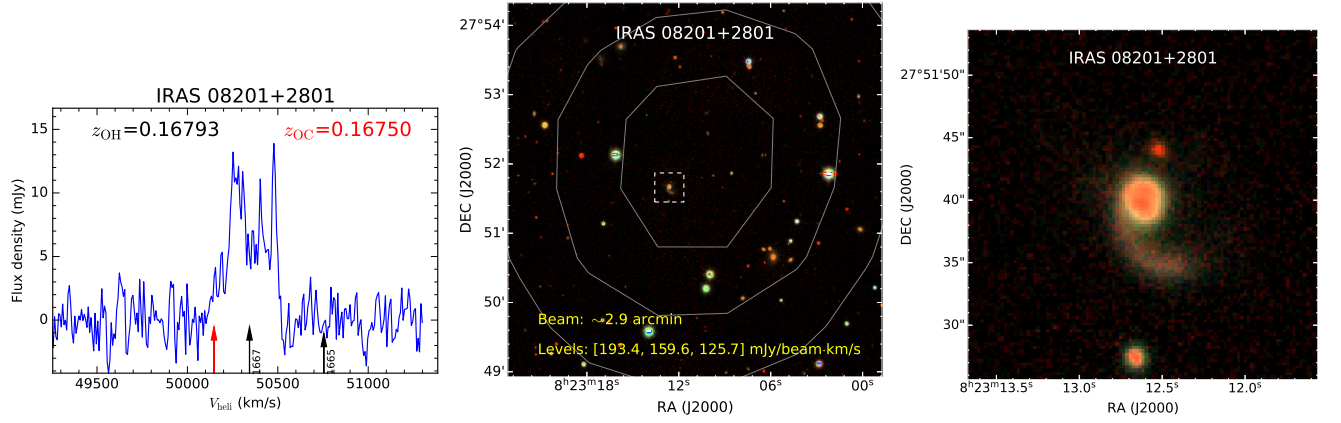


Figure 10. OHM IRAS 08201+2801. Refer to caption in Figure 2

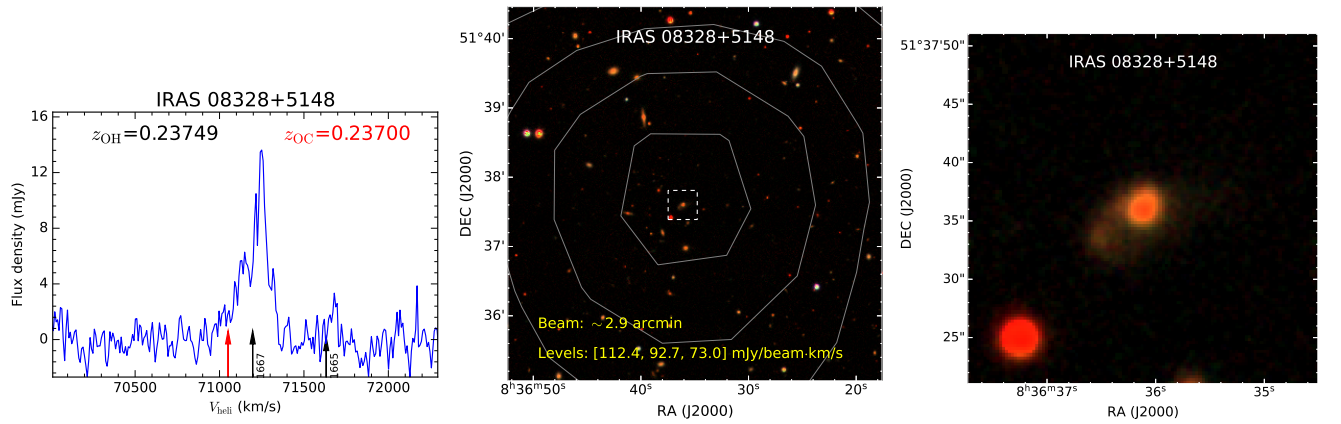


Figure 11. OHM IRAS 08328+5148. Refer to caption in Figure 2

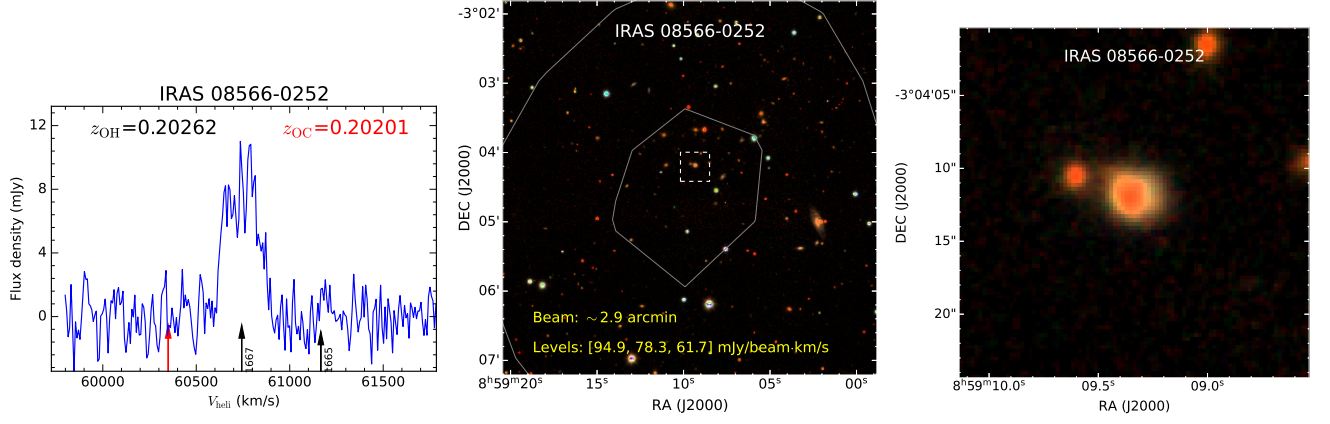


Figure 12. OHM IRAS 08566-0252. Refer to caption in Figure 2

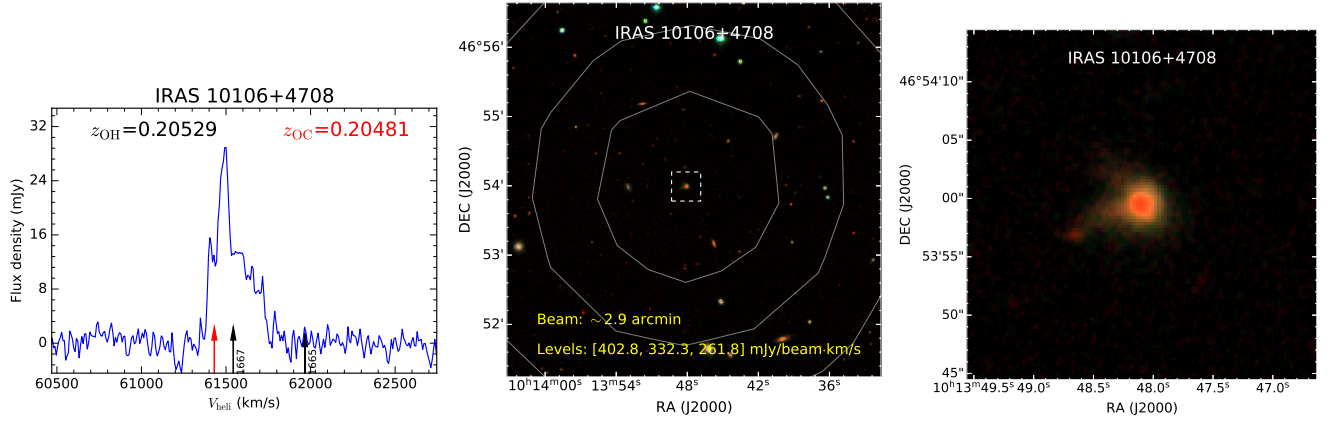


Figure 13. OHM IRAS 10106+4708. Refer to caption in Figure 2

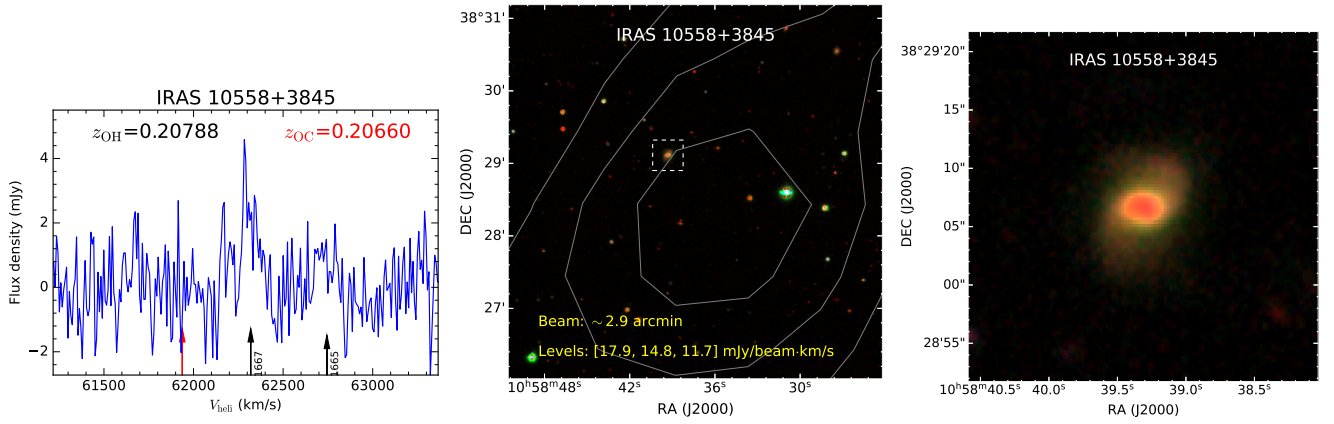


Figure 14. OHM IRAS 10558+3845. Refer to caption in Figure 2

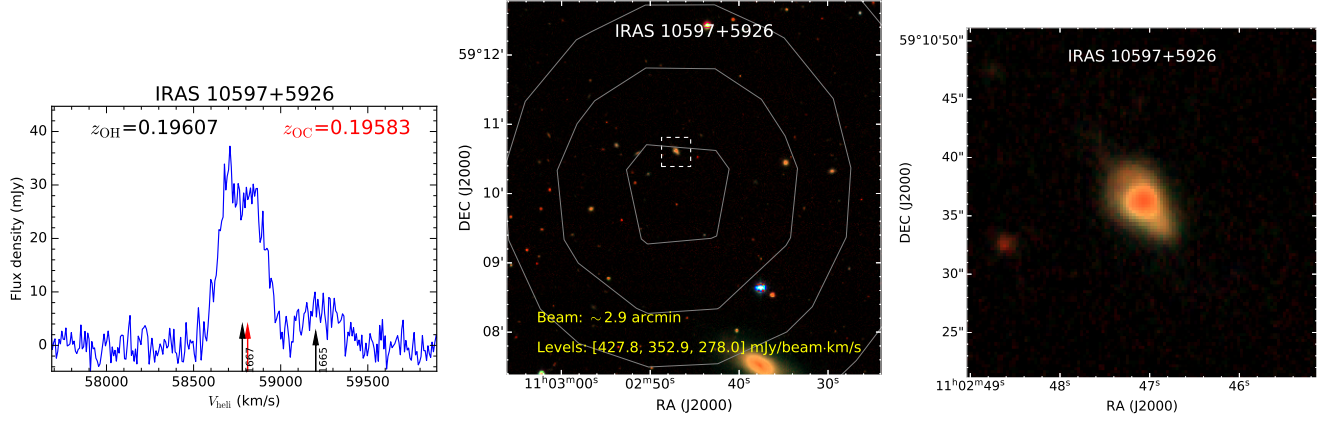


Figure 15. OHM IRAS 10597+5926. Refer to caption in Figure 2

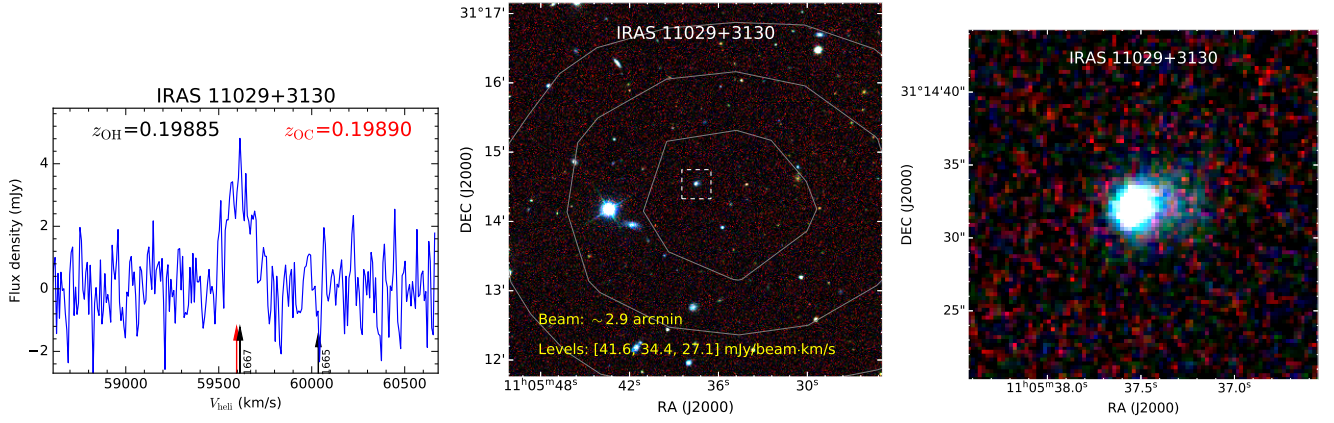


Figure 16. OHM IRAS 11029+3130. Refer to caption in Figure 2

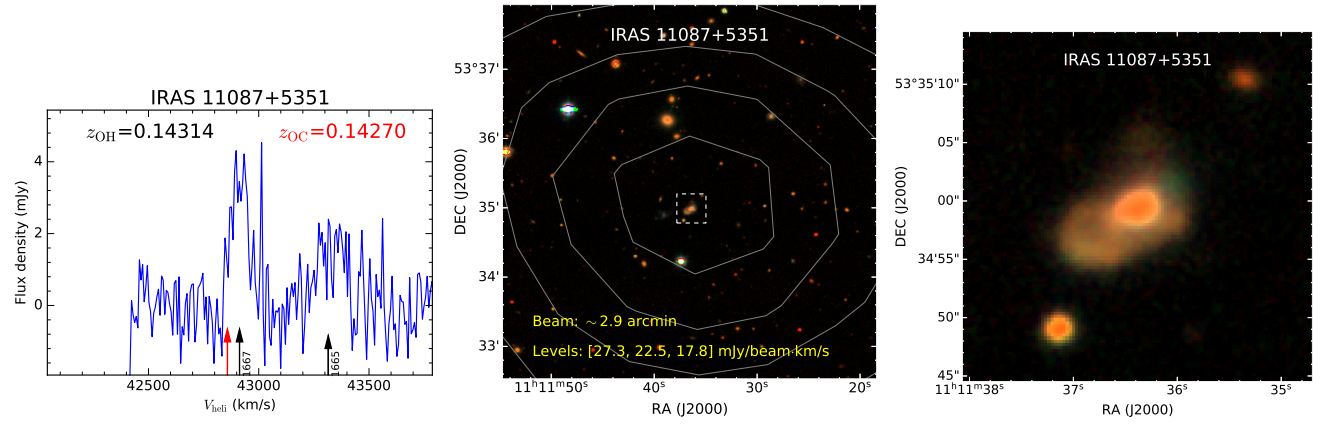


Figure 17. OHM IRAS 11087+5351. Refer to caption in Figure 2

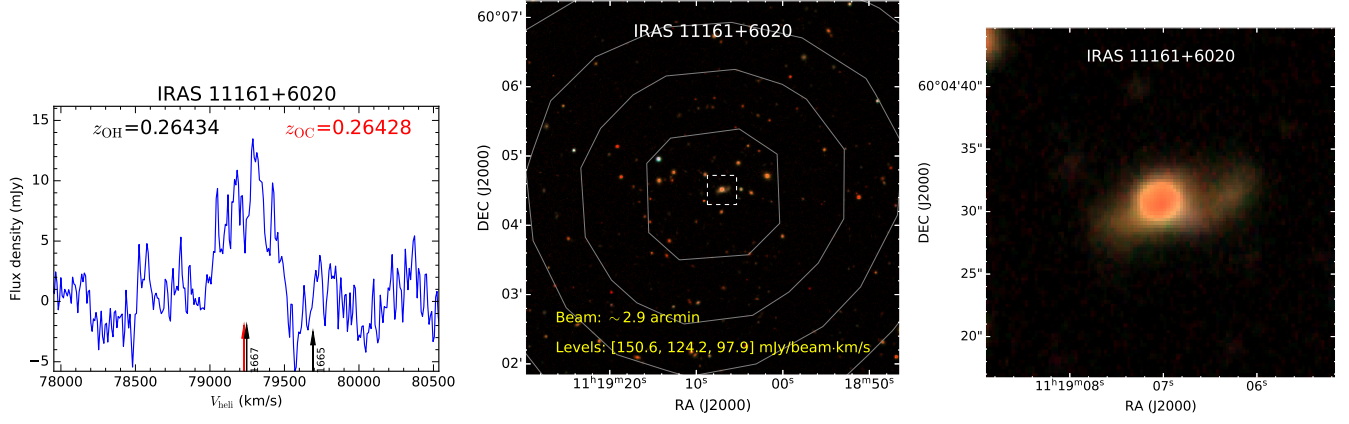


Figure 18. OHM IRAS 11161+6020. Refer to caption in Figure 2

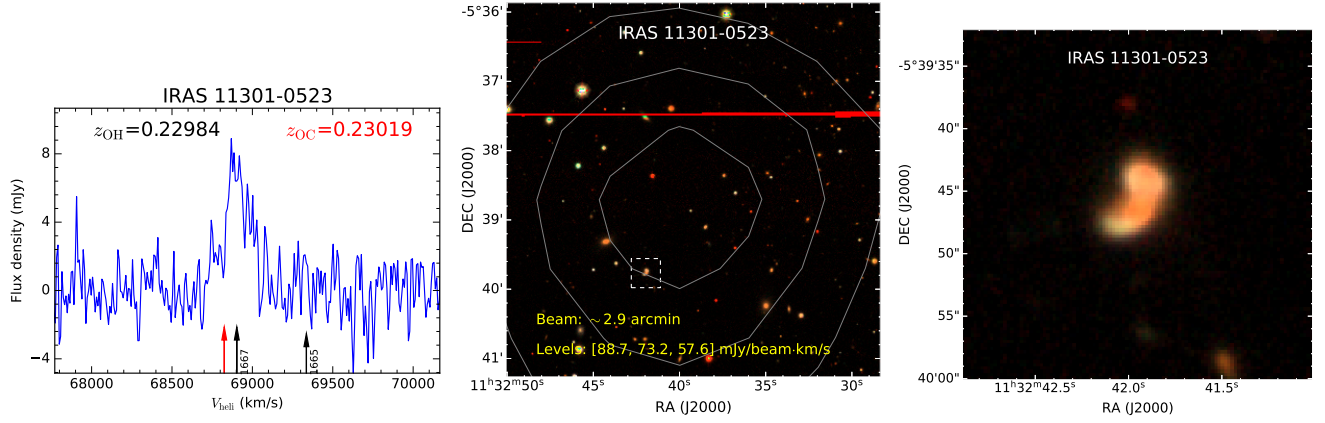


Figure 19. OHM IRAS 11301-0523. Refer to caption in Figure 2

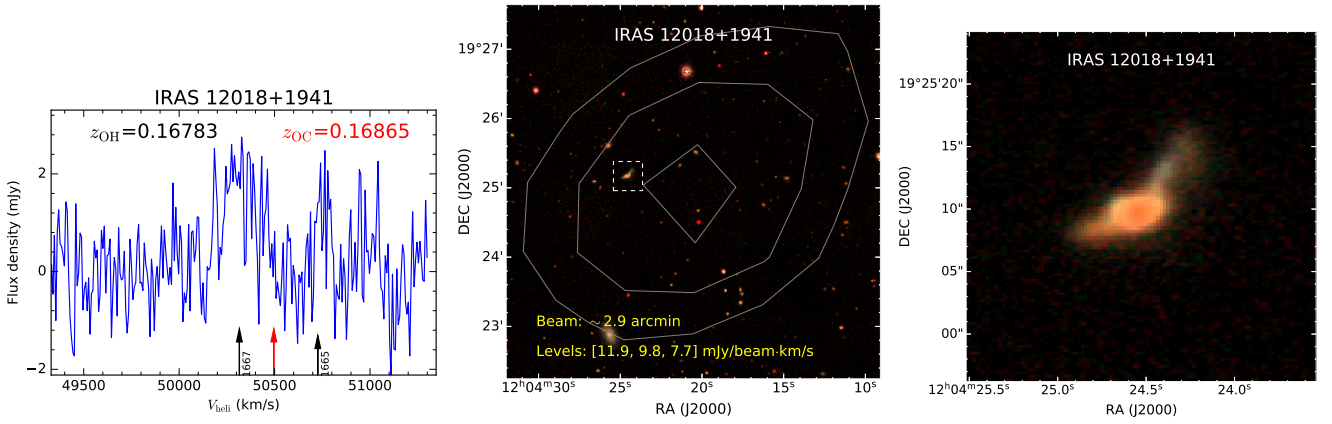


Figure 20. OHM IRAS 12018+1941. Refer to caption in Figure 2

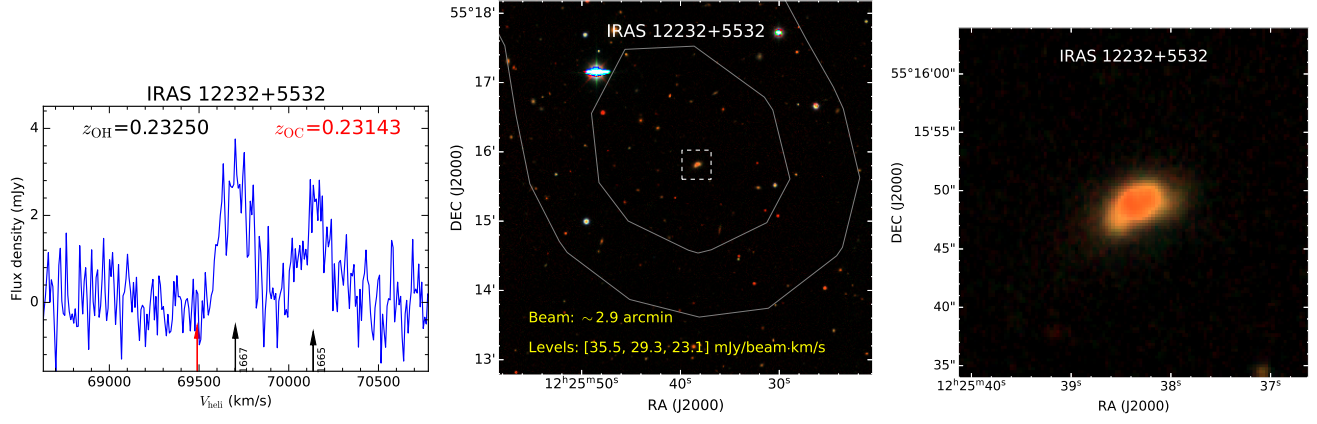


Figure 21. OHM IRAS 12232+5532. Refer to caption in Figure 2

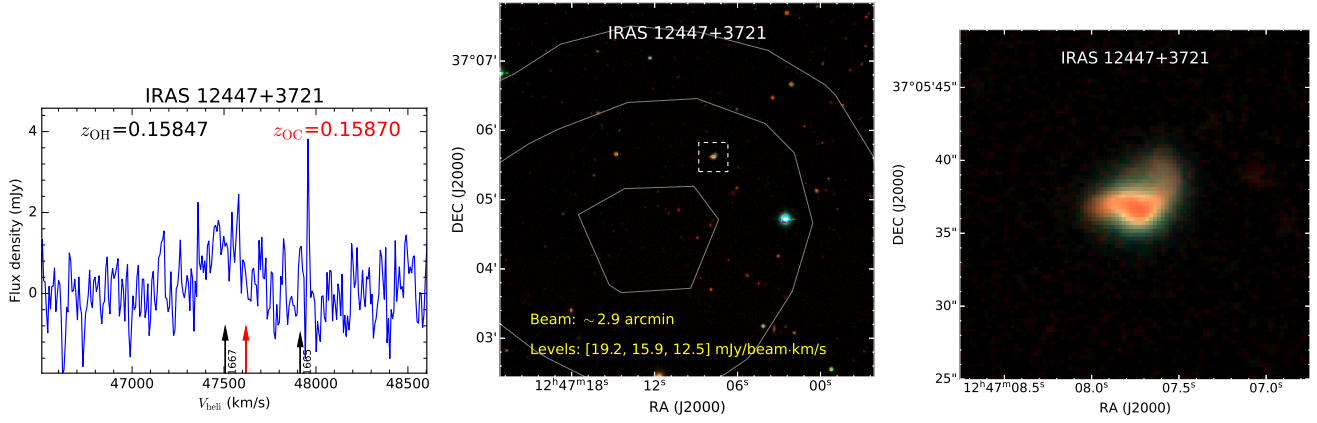


Figure 22. OHM IRAS 12447+3721. Refer to caption in Figure 2

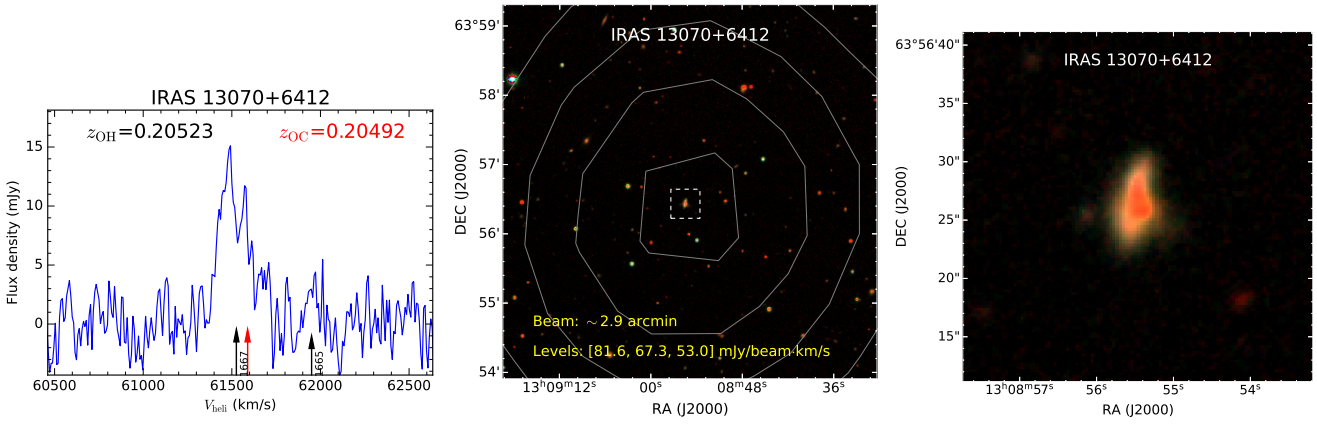


Figure 23. OHM IRAS 13070+6412. Refer to caption in Figure 2

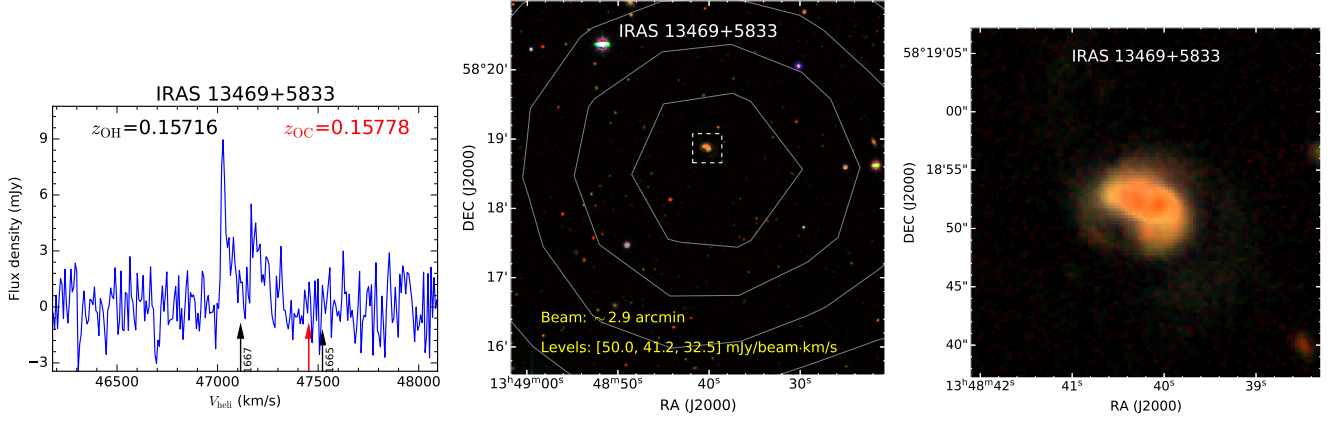


Figure 24. OHM IRAS 13469+5833. Refer to caption in Figure 2

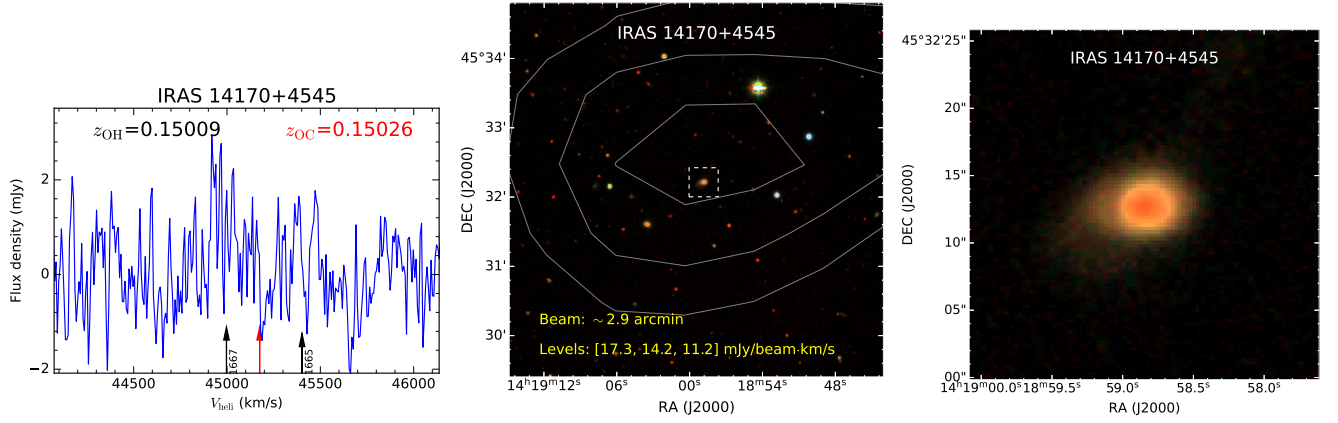


Figure 25. OHM IRAS 14170+4545. Refer to caption in Figure 2

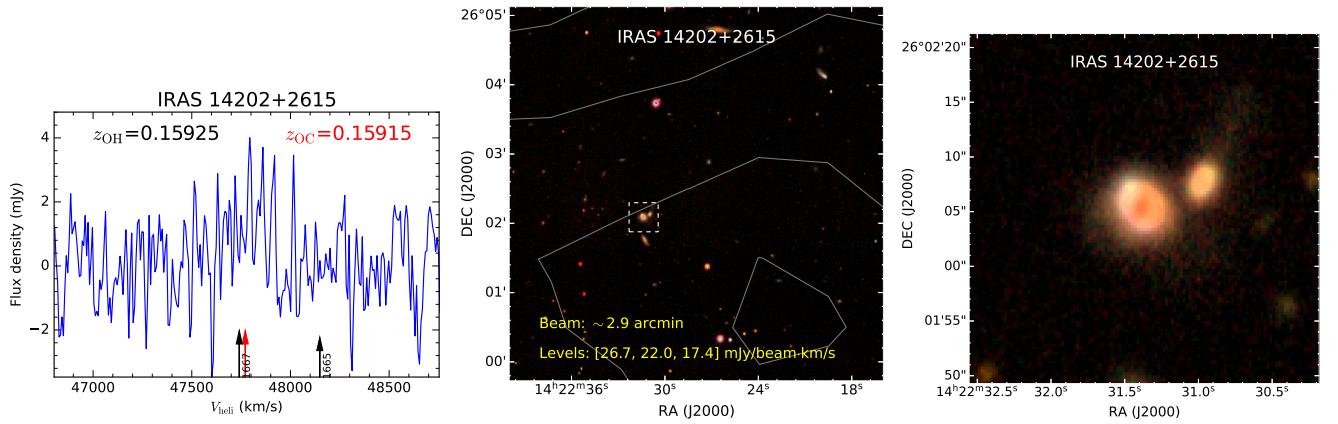


Figure 26. OHM IRAS 14202+2615. Refer to caption in Figure 2

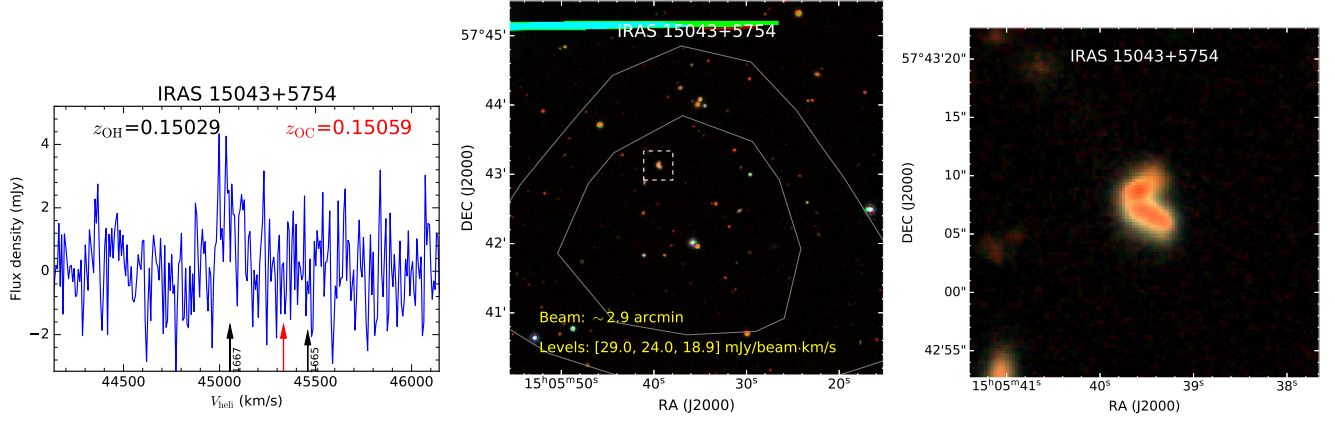


Figure 27. OHM IRAS 15043+5754. Refer to caption in Figure 2

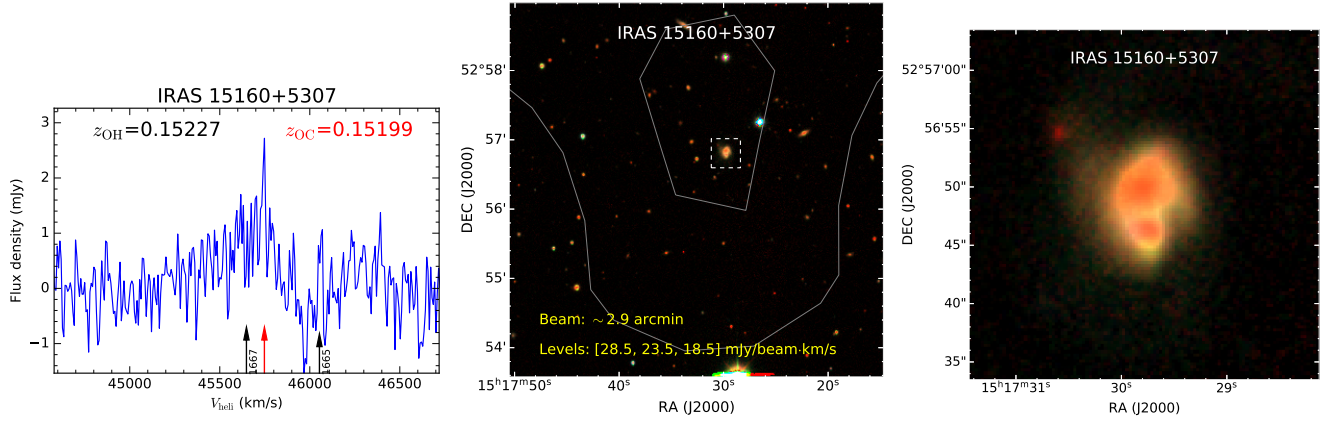


Figure 28. OHM IRAS 15160+5307. Refer to caption in Figure 2

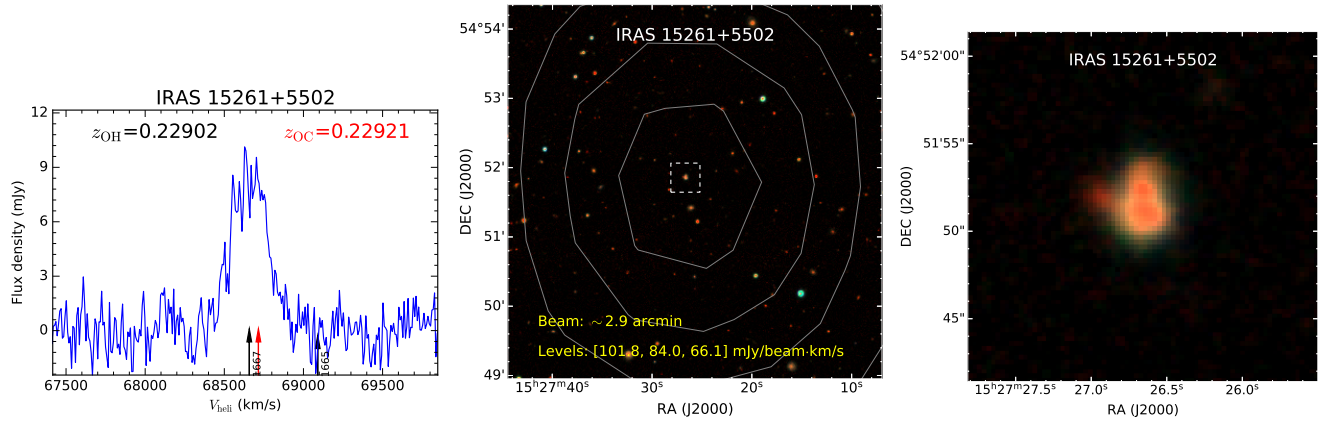


Figure 29. OHM IRAS 15261+5502. Refer to caption in Figure 2

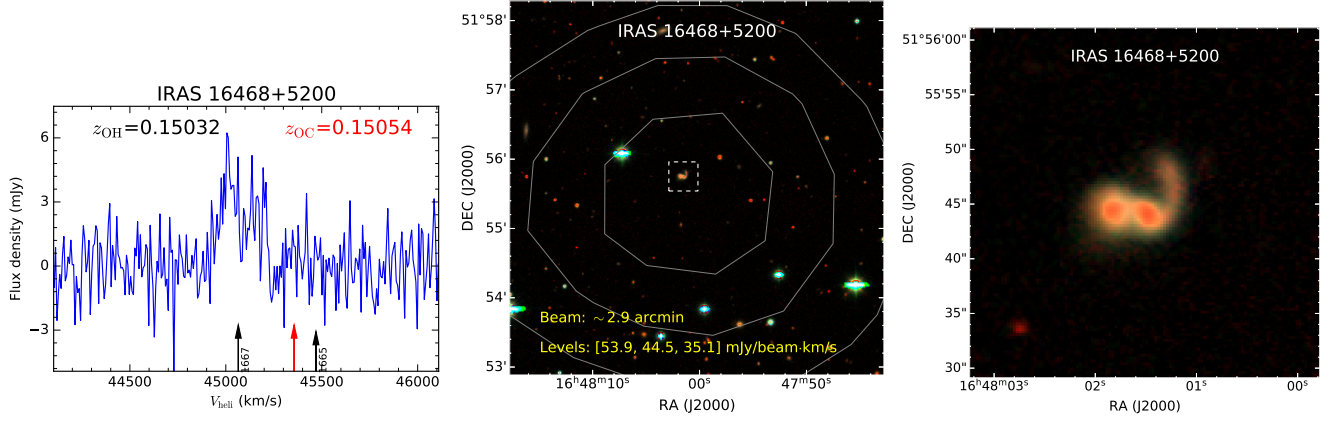


Figure 30. OHM IRAS 16468+5200. Refer to caption in Figure 2

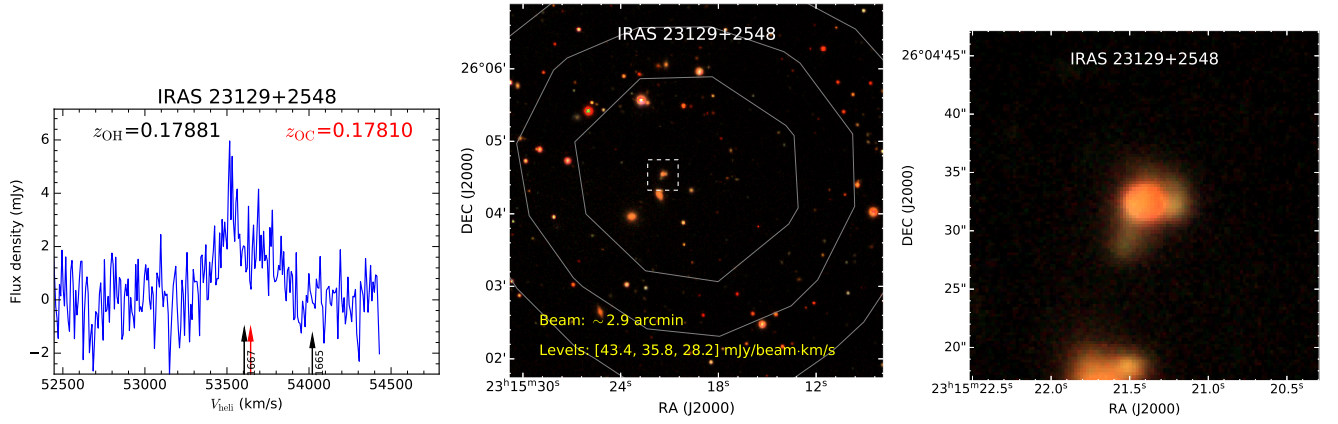


Figure 31. OHM IRAS 23129+2548. Refer to caption in Figure 2